Thermochemical Non-Equilibrium Entry Flows in Mars in Two-Dimensions – Part II

EDISSON SÁVIO DE GÓES MACIEL[(1)] and AMILCAR PORTO PIMENTA[(2)]
IEA – Aeronautical Engineering Division
ITA – Aeronautical Technological Institute
Praça Mal. do Ar Eduardo Gomes, 50 – Vila das Acácias – São José dos Campos – SP – 12228-900
BRAZIL
[(1)]edisavio@edissonsavio.eng.br [(1)]http://www.edissonsavio.eng.br and [(2)]amilcar@ita.br

Abstract: - This work, second part of this study, describes the numerical results obtained by thermochemical non-equilibrium simulations of reactive flow in two-dimensions. The Van Leer and Liou and Steffen Jr. schemes, in their first- and second-order versions, are implemented to accomplish the numerical simulations. The Euler and Navier-Stokes equations, on a finite volume context and employing structured spatial discretization, are applied to solve the "hot gas" hypersonic flows around a double ellipse, around an entry capsule, and around a pathfinder in two-dimensions. The second-order version of the Van Leer and Liou and Steffen Jr. schemes are obtained from a "MUSCL" extrapolation procedure in a context of structured spatial discretization. The convergence process is accelerated to the steady state condition through a spatially variable time step procedure, which has proved effective gains in terms of computational acceleration (Maciel). The reactive simulations involve a Mars atmosphere chemical model of nine species: N, O, N_2, O_2, NO, CO_2, C, CO, and CN, based on the work of Kay and Netterfield. Fifty-three chemical reactions, involving dissociation and recombination, are simulated by the proposed model. The Arrhenius formula is employed to determine the reaction rates and the law of mass action is used to determine the source terms of each gas species equation. The results have indicated the Van Leer scheme as the most accurate one, both inviscid and viscous cases.

Key-Words: - Thermochemical non-equilibrium, Mars entry, Nine species model, Hypersonic "hot gas" flow, Finite volume, Euler and Navier-Stokes equations, Two-dimensions.

1 Introduction

There has been significant interest in recent years in a mission to Mars. One such proposal is the MARSNET assessment study [1] concerning the potential contribution of ESA (European Space Agency) to a Mars Network mission in cooperation with NASA. NASA is currently studying a network mission MESUR (Mars Environmental Survey), involving the placement of up twenty small scientific stations on the surface of Mars. The objective of the proposed ESA activities is the provision of three of these stations to perform a variety of scientific experiments. The intended entry scenario is an unguided ballistic entry at a typical velocity of 6 km/s using a blunt sphere/cone configuration in which deceleration is provided predominantly by hypersonic aero-braking. It is important that the mass of the vehicle structure and thermal protection system (TPS) be minimized such that the payload delivered to the surface may be maximized.

The trajectory for a ballistic Martian entry takes the vehicle through regions where thermochemical non-equilibrium effects in the surrounding shock layer may be significant. For typical entry velocities (> 5 km/s) the temperature in the shock layer will be sufficiently high for dissociation of the freestream species to occur. The energy removed through such reactions may be released at the vehicle surface via recombination leading to significantly enhanced heat transfer rates. In order to design the TPS for minimum mass the heat transfer rate needs to be accurately predicted. This requires that any catalytic properties of the TPS material are accounted for in the heat transfer rate calculation since these will determine the extent of wall recombination.

As aforementioned, missions to other planets remain an objective for the ESA, and such missions generally involve the entry of a space vehicle into the atmospheres of those planets. In the context of such entry, aerothermodynamics is one of the critical technologies. While the thermochemical behavior of air under re-entry conditions has been studied extensively, and is to some degree understood, the same is not true for entries into other atmospheres. The atmospheres of Mars and Venus, for example, contain significant amounts of carbon dioxide. In particular, the Mars atmosphere is a mixture of approximately 96% CO_2 and 4% N_2, with pressures much lower than the Earth's

atmosphere, so for any entry into the Martian atmosphere the non-equilibrium behavior of CO_2 is likely to be of importance for a typical blunt body entry vehicle. This includes not just the influence of thermochemistry on the forebody heatshield flowfield, but also the influence on the shoulder expansion, base flow, and base heating environment.

Analyzing the reentry flows in Earth, [2] have proposed a numerical tool implemented to simulate inviscid and viscous flows employing the reactive gas formulation of thermal and chemical non-equilibrium. The Euler and Navier-Stokes equations, employing a finite volume formulation, on the context of structured and unstructured spatial discretizations, were solved. These variants allowed an effective comparison between the two types of spatial discretization aiming verify their potentialities: solution quality, convergence speed, computational cost, etc. The aerospace problem involving the hypersonic flow around a blunt body, in two-dimensions, was simulated. The reactive simulations involved an air chemical model of five species: N, O, N_2, O_2 and NO. Seventeen chemical reactions, involving dissociation and recombination, were simulated by the proposed model. The Arrhenius formula was employed to determine the reaction rates and the law of mass action was used to determine the source terms of each gas species equation. Good results were obtained with such code.

This work, second part of this study, describes the numerical results obtained by thermochemical non-equilibrium simulations of reactive flow in two-dimensions. The [3-4] schemes, in their first- and second-order versions, are implemented to accomplish the numerical simulations. The Euler and Navier-Stokes equations, on a finite volume context and employing structured spatial discretization, are applied to solve the “hot gas” hypersonic flows around a double ellipse, around an entry capsule, and around a pathfinder configuration, in two-dimensions. The second-order versions of the [3-4] schemes are obtained from a “MUSCL” extrapolation procedure (details in [5]) in a context of structured spatial discretization. The convergence process is accelerated to the steady state condition through a spatially variable time step procedure, which has proved effective gains in terms of computational acceleration (see [6-7]).

The reactive simulations involve a Mars atmosphere chemical model of nine species: N, O, N_2, O_2, NO, CO_2, C, CO, and CN. Fifty-three chemical reactions, involving dissociation and recombination, are simulated by the proposed model. The Arrhenius formula is employed to determine the reaction rates and the law of mass action is used to determine the source terms of each gas species equation.

In this paper, the double ellipse, the entry capsule and the pathfinder solutions are presented. The results have demonstrated that the most correct aerodynamic coefficient of lift is found in the pathfinder problem and is obtained by the [3] scheme, with first-order accuracy, in an inviscid formulation, to a reactive condition of thermochemical non-equilibrium.

2 Results

Tests were performed in a notebook with INTEL PENTIUM Dual Core processors of 2.30GHz and 2GBytes of RAM. As the interest of this work is steady state problems, it is necessary to define a criterion which guarantees the convergence of the numerical results. The criterion adopted was to consider a reduction of no minimal three (3) orders of magnitude in the value of the maximum residual in the calculation domain, a typical CFD-community criterion. In the simulations, the attack angle was set equal to zero.

2.1 Double Ellipse Problem

The initial conditions are presented in Tab. 1. The Reynolds number is obtained from data available in the Mars atmosphere tables [8]. The geometry of this problem is a double ellipse, described in [9]. The far field is located at 5.0 times the biggest semi-axis length of the biggest ellipse.

The double ellipse mesh is composed of 3,528 rectangular cells and 3,650 nodes in the structured case. To the generated meshes and the boundary conditions the reader is encouraged to read [9].

2.1.1. Inviscid, first order, structured results

Figure 1 exhibits the pressure contours obtained by the [3] scheme. The pressure peak at the configuration nose is 516.16 unities. The shock waves at the bigger ellipse (first ellipse) and at the minor ellipse (second ellipse) are well captured. The interference between the shock waves at the double ellipse upper surface is also well captured by the [3] algorithm.

Figure 2 shows the pressure contours obtained by the [4] scheme. The pressure peak occurs at the first ellipse (biggest ellipse) nose and has 577.96 unities, which is bigger than the respective result obtained by the [3] scheme. Moreover, the shock wave is closer to the blunt nose in the [4] solution than in the [3] solution. The shock interference close to the

second ellipse (minor ellipse) is weaker, but is well captured by the [4] algorithm.

Table 1. Initial conditions to the double ellipse problem.

Property	Value
M_∞	26.0
ρ_∞	0.000265 kg/m^3
p_∞	8.1394 Pa
U_∞	5,210 m/s
T_∞	160.0 K
Altitude	44,000 m
c_N	0.00
c_O	0.00
c_{N_2}	0.0270
c_{O_2}	0.0015
c_{NO}	0.00
c_{CO_2}	0.9715
c_C	0.00
c_{CO}	0.00
c_{CN}	0.00
L	5.0 m
Re_∞	8.04x10^5

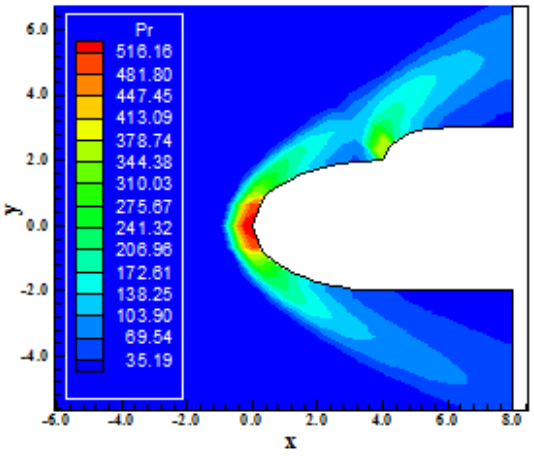

Figure 1. Pressure contours ([3]).

Figure 3 presents the Mach number field generated by the [3] scheme. The Mach number peak has the value 23.56. Figure 4 shows the Mach number field obtained by the [4] scheme. Its Mach number peak has a value of 23.56, equal to the value obtained with the [3] scheme. Comparing the shock stand-off distance between the [3] and [4] solution, it is clear that the [4] solution is closer to the first ellipse nose than the [3] solution.

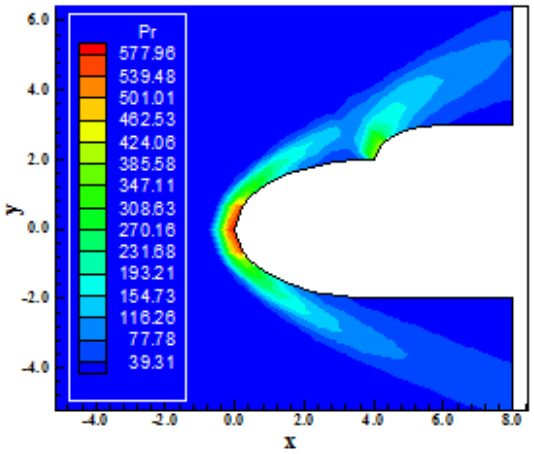

Figure 2. Pressure contours ([4]).

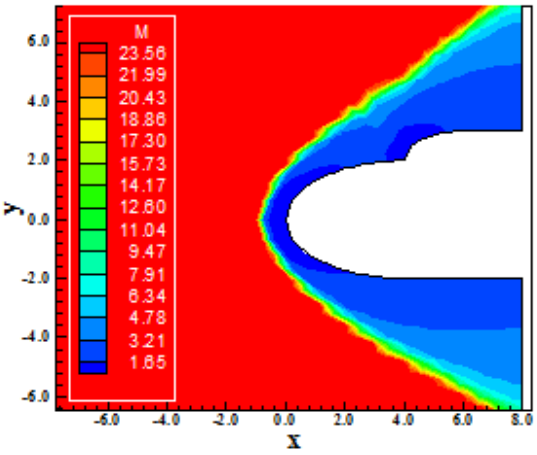

Figure 3. Mach number contours ([3]).

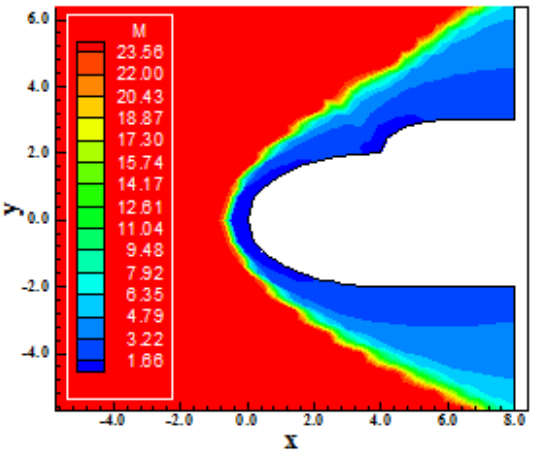

Figure 4. Mach number contours ([4]).

Figures 5 and 6 exhibit the translational / rotational temperature contours obtained by the [3-4] schemes, respectively. The temperature field obtained by the [3] algorithm is more severe than

the respective temperature field obtained by the [4] algorithm.

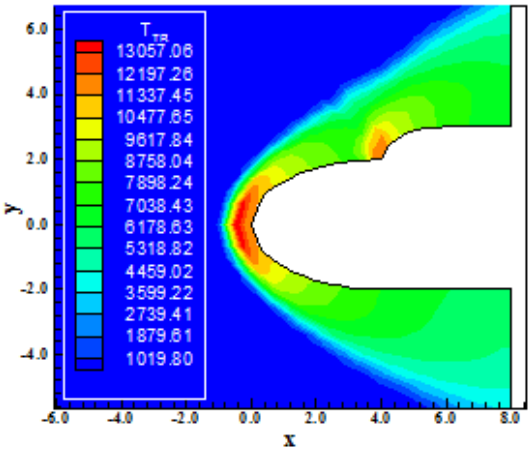

Figure 5. Translational/Rotational temperature contours ([3]).

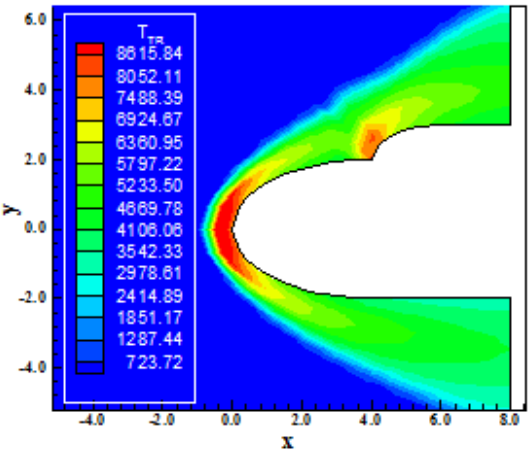

Figure 6. Translational/Rotational temperature contours ([4]).

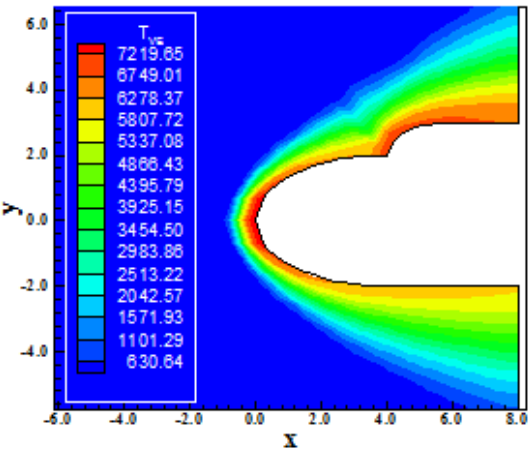

Figure 7. Vibrational temperature contours ([3]).

Although the former present a bigger temperature field, the latter presents bigger region of high temperature, which can influence the species mass fraction distributions.

Figures 7 and 8 show the vibrational temperature distributions obtained by the [3-4] algorithms, respectively. Both fields present similar distributions. The shock stand-off distance is again minor to the [4] solution than the [3] solution.

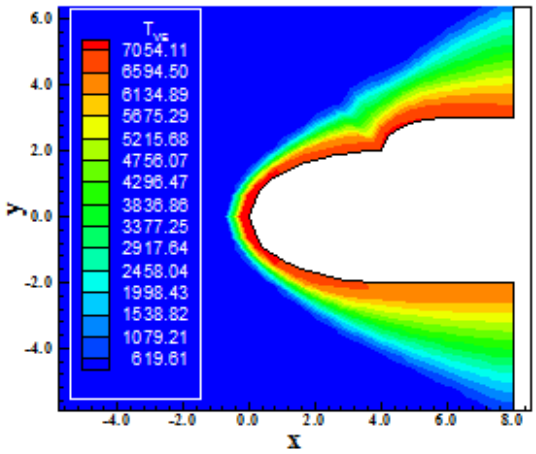

Figure 8. Vibrational temperature contours ([4]).

Figure 9 exhibits the species mass fraction distributions obtained by the [3] algorithm. As can be seen, there is a significant dissociation of CO_2 with the consequent formation of CO and O. Figure 10 shows the species mass fraction distributions generated by the [4] algorithm. In this case, there is a considerable dissociation of CO_2 and a significant formation of CO and O. The [4] scheme captures a bigger formation of CO and O than the [3] scheme.

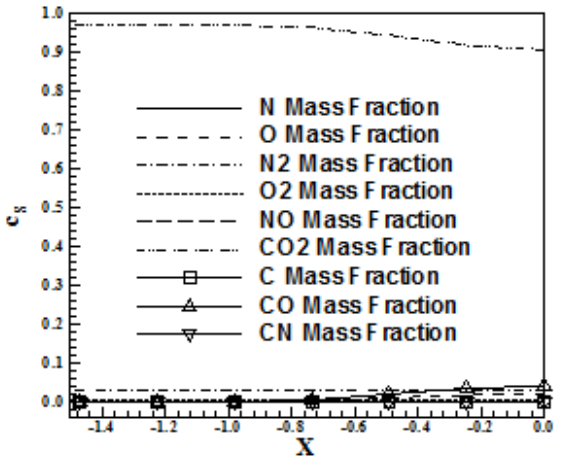

Figure 9. Species mass fraction distributions at the stagnation line ([3]).

It can be originated from the bigger region of translational/rotational temperature field observed in Fig. 6, where it was emphasized that such behaviour could influence the species mass fraction distributions, as really occurred.

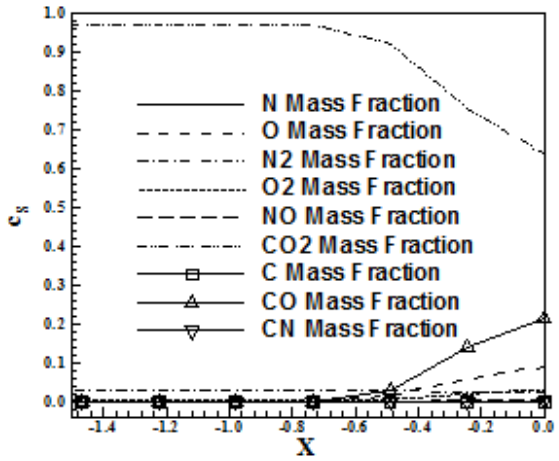

Figure 10. Species mass fraction distributions at the stagnation line ([4]).

2.1.2. Viscous, first order, structured results

Figures 11 and 12 show the pressure contours obtained by the [3-4] schemes, in their first order, viscous case. The pressure peak generated by the [3] scheme is more strength than the respective generated by the [4] scheme. The shock interference is also better described by the [3] solution. The shock stand-off distance is very close to the blunt nose in the [4] solution, which detects a minor shock interference close to the second ellipse.

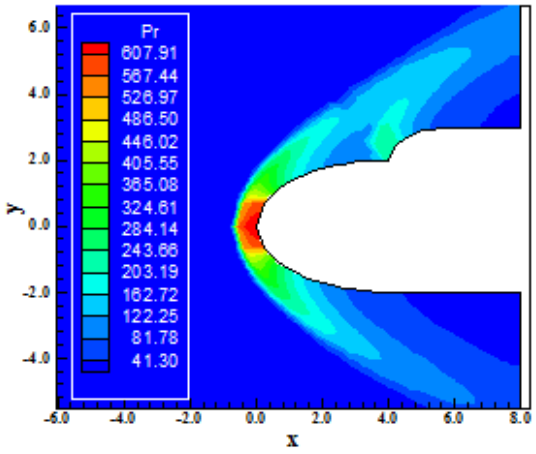

Figure 11. Pressure contours ([3]).

Figures 13 and 14 presents the Mach number fields generated by the [3-4] algorithms, in their first order, viscous case. Both solutions present the same Mach number peak, as also the same Mach number field. The shock wave develops naturally: normal shock, oblique shocks and Mach waves.

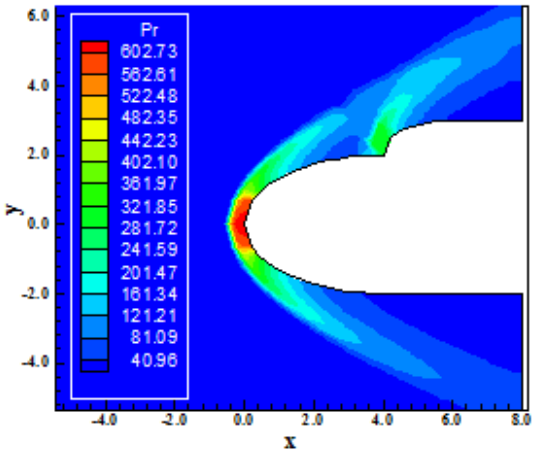

Figure 12. Pressure contours ([4]).

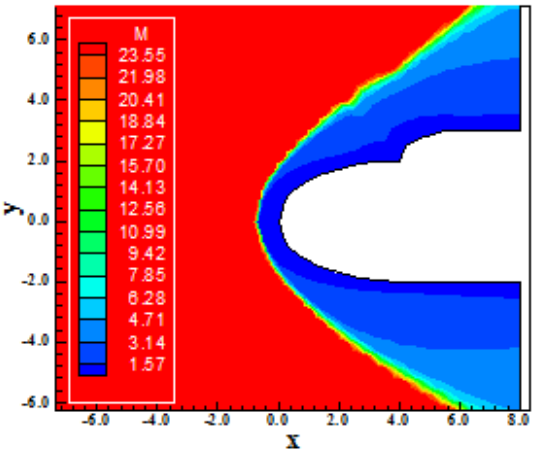

Figure 13. Mach number contours ([3]).

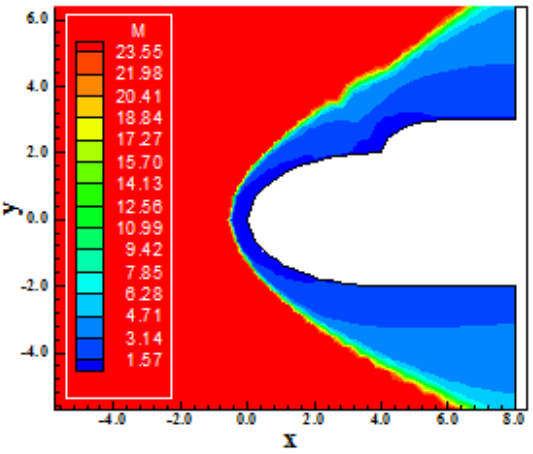

Figure 14. Mach number contours ([4]).

Figures 15 and 16 exhibit the translational / rotational temperature contours generated by the [3-4] algorithms, respectively. As can be seen, the temperature field resulting from [3] is more intense than the respective generated by [4], but the

differences between these values and those obtained in the first order inviscid case are small.

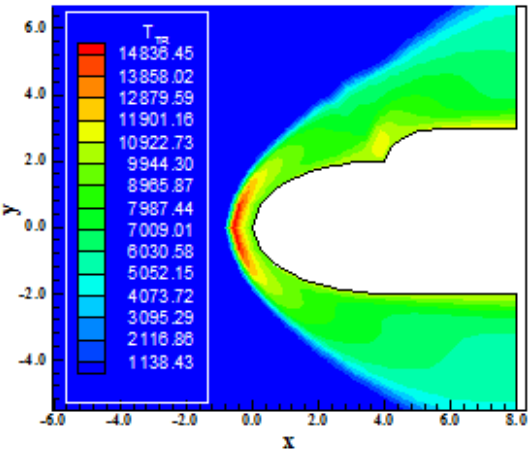

Figure 15. Translational/Rotational temperature contours ([3]).

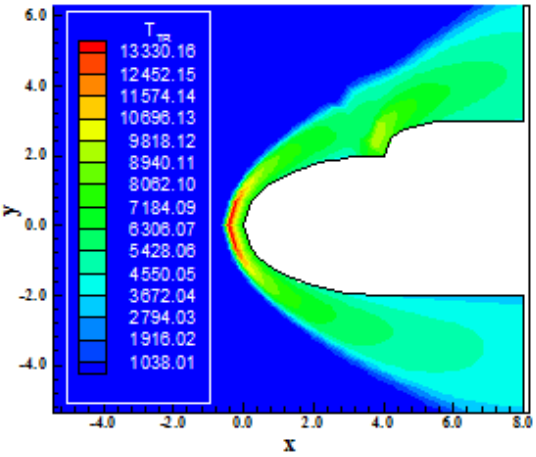

Figure 16. Translational/Rotational temperature contours ([4]).

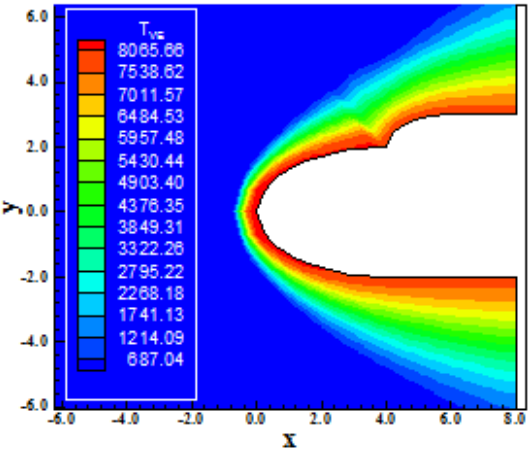

Figure 17. Vibrational temperature contours ([3]).

Figures 17 and 18 show the vibrational temperature contours obtained by the [3-4] schemes, respectively. The difference between these two fields is very small. It is possible to assure that the viscous formulation allows the two schemes to capture practically the same fields, converging to a same solution. Qualitatively, the two solutions are very close.

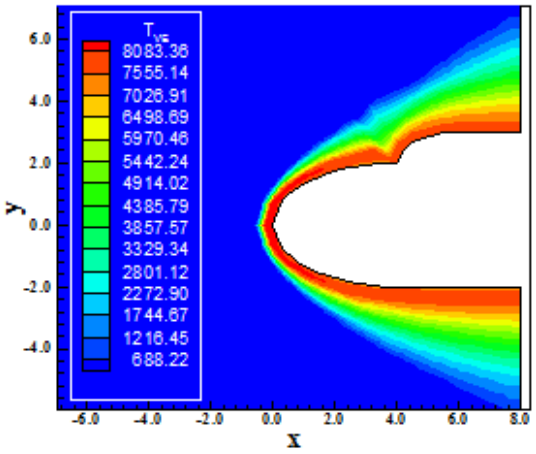

Figure 18. Vibrational temperature contours ([4]).

Figure 19 presents the species mass fraction distributions at the stagnation line generated by the [3] algorithm. As can be seen, good dissociation of the CO_2 is observed, as also a considerable formation of CO and of O. Figure 20 exhibits the species mass fraction distributions generated by the [4] algorithm. As can be noted, a considerable formation of CO and of O is formed at the expense of CO_2 dissociation. Both solutions present more formation of CO and of O in relation to the first order inviscid case. It is clear that the viscous effects are predominant in this solution and is responsible by the solution quality and quantity.

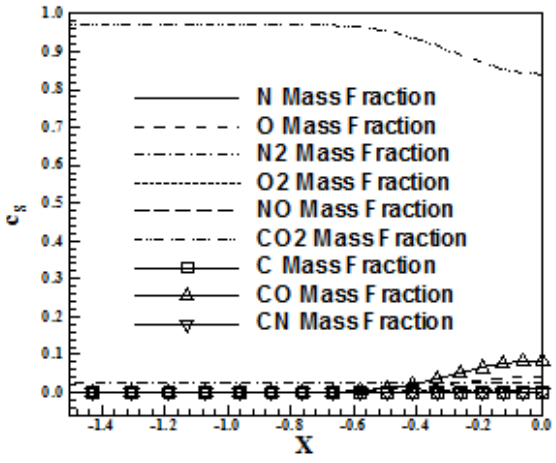

Figure 19. Species mass fraction distributions at the stagnation line ([3]).

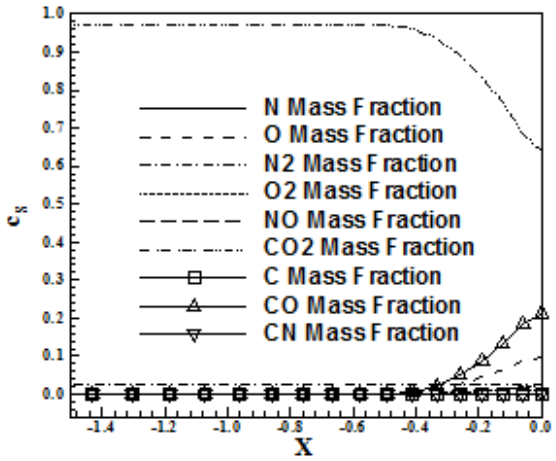

Figure 20. Species mass fraction distributions at the stagnation line ([4]).

2.1.3. Inviscid, second order, structured results

For these results, only the [3] scheme yielded converged solutions. Figure 21 exhibits the pressure contours generated by the [3] algorithm. Its pressure peak reaches the value of 537.74 unities, bigger than the respective first order inviscid solution.

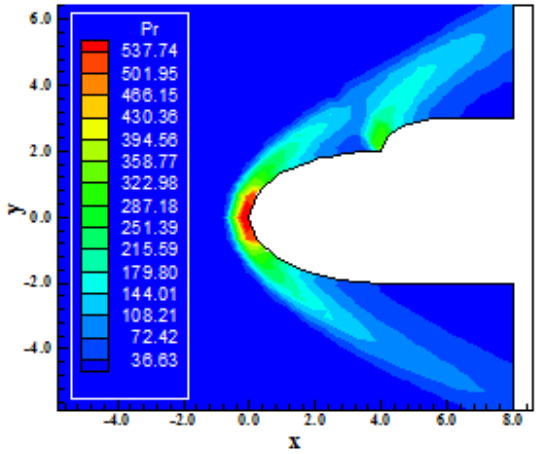

Figure 21. Pressure contours ([3]).

Figure 22 shows the Mach number contours generated by the [3] algorithm. The Mach number peak presents the value of 23.56, the same obtained by the first order inviscid solution. The shock wave presents the expected behaviour: passing from a normal shock to a Mach wave, through oblique shock waves.

Figure 23 presents the translational/rotational temperature contours obtained by the [3] scheme, in its second order inviscid solution. The temperature peak is less than the respective solution in the first order inviscid case.

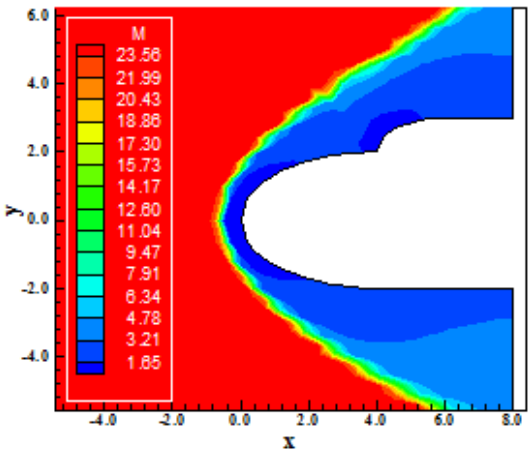

Figure 22. Mach number contours.

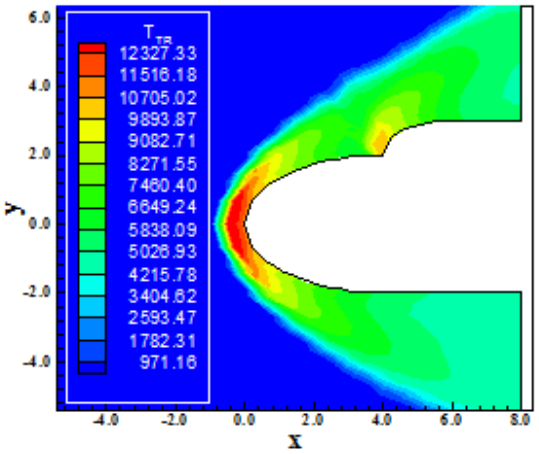

Figure 23. Translational/Rotational temperature contours ([3]).

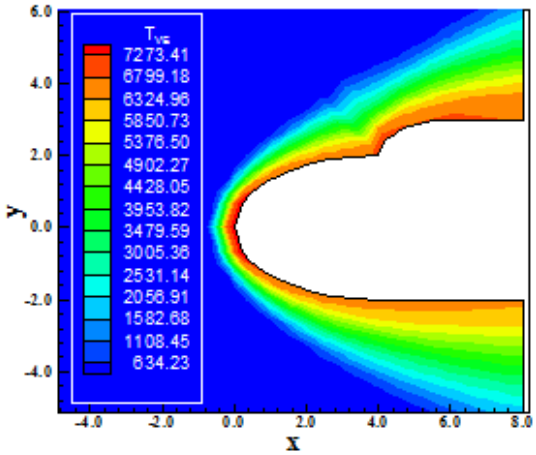

Figure 24. Vibrational temperature contours ([3]).

Figure 24 exhibits the vibrational temperature contours and agrees with the inviscid first order behaviour. The maximum vibrational temperature reaches a value of 7,273.41 K, which is close to the first order inviscid solution.

Figure 25 exhibits the species mass fraction distributions at the stagnation line generated by the [3] scheme. A significant dissociation of CO_2 gives raise to the formation of CO and O, in a more pronounced way. This behaviour is very close to its first order inviscid counterpart.

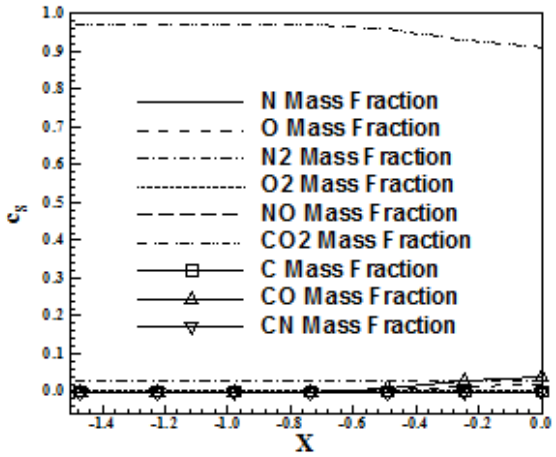

Figure 25. Species mass fraction distributions at the stagnation line ([3]).

In spite of the non-convergence of the [4] algorithm, the results obtained with the [3] algorithm are encouraging and serves as a point of comparison to other methods and limiters.

2.1.4. Viscous, second order, structured results

In this case, only the [3] algorithm yielded converged results. Figure 26 exhibits the pressure contours obtained by the [3] scheme.

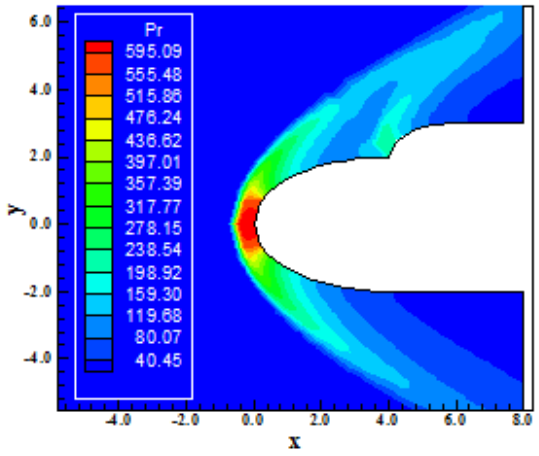

Figure 26. Pressure contours ([3]).

The pressure peak reaches a maximum value of 595.09 unities, lower than the respective value of the [3] first order results. Figure 27 shows the Mach number contours generated by the [3] scheme. The contour curves present the appropriated properties: normal shock wave ahead of the blunt nose of the first ellipse, oblique shock waves close to the body and Mach waves far from the body.

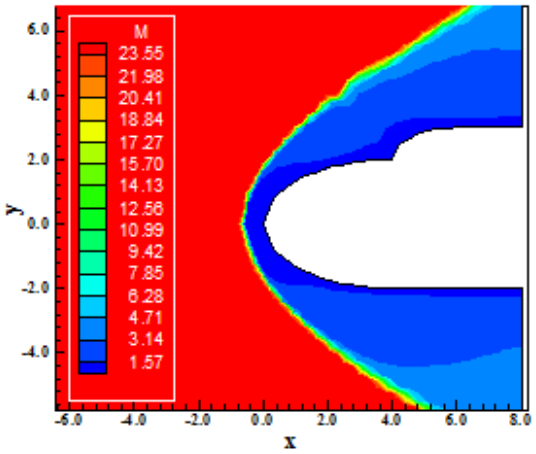

Figure 27. Mach number contours ([3]).

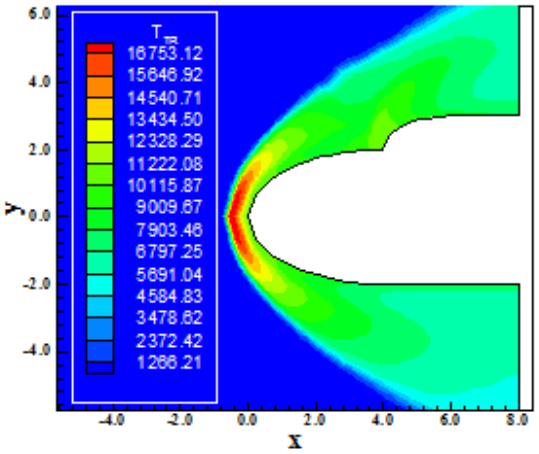

Figure 28. Translational/Rotational temperature contours ([3]).

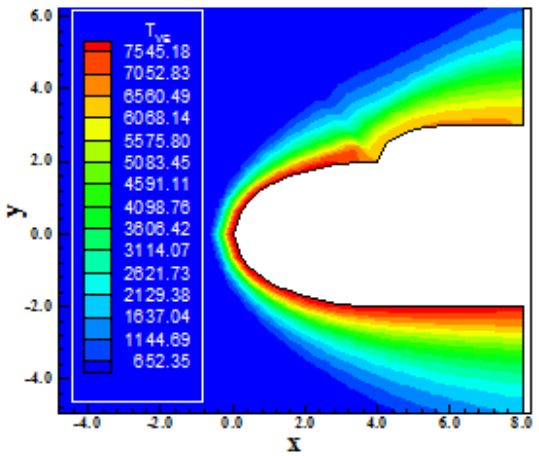

Figure 29. Vibrational temperature contours ([3]).

Figure 28 presents the translational/rotational temperature contours obtained by the [3] scheme. The translational/rotational temperature peak reaches a maximum of 16,753.12 K, close to the double ellipse blunt nose. It is a high temperature, but agrees with the expected temperature at the Mars atmosphere to the given initial conditions.

Figure 29 exhibits the vibrational temperature contours. As can be seen the vibrational temperature peak assumes the value of 7,545.18 K, which agrees with the expected behavior of this atmosphere (the translational/rotational temperature being almost the double of the vibrational temperature).

Figure 30 shows the species mass fraction distributions at the stagnation line generated by the [3] scheme. A discrete increasing of the CO formation due to CO_2 dissociation is perceptible. The formation of O is practically non-perceptible.

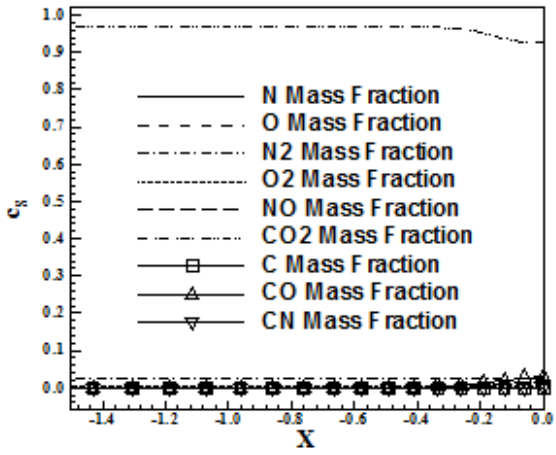

Figure 30. Species mass fraction distributions at the stagnation line ([3]).

2.2 Entry Capsule Problem

The initial conditions are presented in Tab. 2. The Reynolds number is obtained from data available in the Mars atmosphere tables [8]. The geometry of this problem is an entry capsule, described in [9]. The far field is located at 30.0 times the lowest semi-axis length of the elliptical surface.

The entry capsule is composed of 3,136 rectangular cells and 3,250 nodes in the structured case. To the generated meshes and the boundary conditions the reader is encouraged to read [9]. Only one boundary condition is not described in this reference: the condition for the trailing edge wake. The Kutta condition imposes continuity of the flow at the wake. Hence, the vector of conserved variables should be equal at the upper and lower sides of the wake. This imposition satisfies the flow continuity at such boundary.

Table 2. Initial conditions to the entry capsule problem.

Property	Value
M_∞	26.0
ρ_∞	0.000265 kg/m^3
p_∞	8.1394 Pa
U_∞	5,210 m/s
T_∞	160.0 K
Altitude	44,000 m
c_N	0.00
c_O	0.00
c_{N_2}	0.0270
c_{O_2}	0.0015
c_{NO}	0.00
c_{CO_2}	0.9715
c_C	0.00
c_{CO}	0.00
c_{CN}	0.00
L	3.0 m
Re_∞	4.83x10^5

It is important to emphasize that although the initial conditions are the same of the double ellipse problem, the characteristic length and the Reynolds number is not. So, the problem is different.

2.2.1. Inviscid, first order, structured results

Figures 31 and 32 exhibit the pressure contours generated by [3-4] algorithms, respectively. The pressure peak of the [3] solution is equal to 596.49 unities, whereas the [4] solution presents a pressure peak of 623.89 unities. The [4] solution is more conservative than the [3] solution.

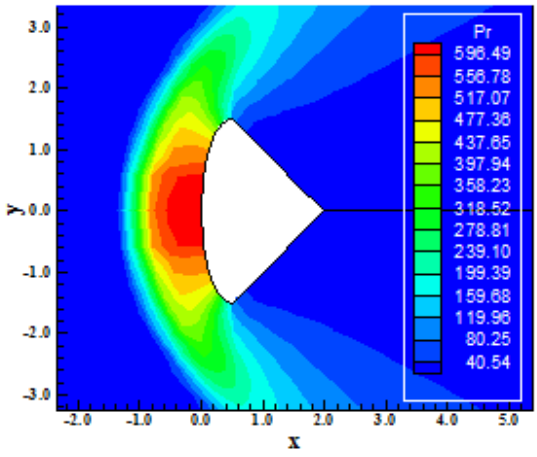

Figure 31. Pressure contours ([3]).

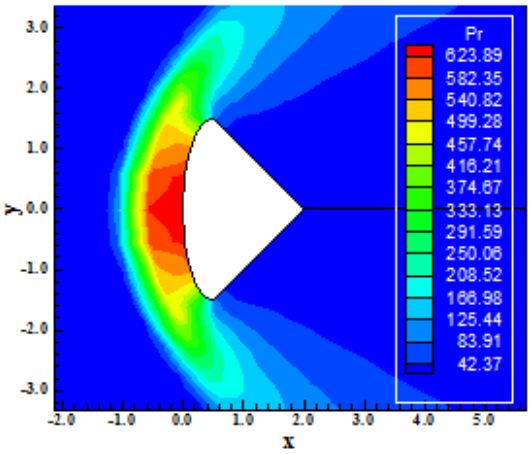

Figure 32. Pressure contours ([4]).

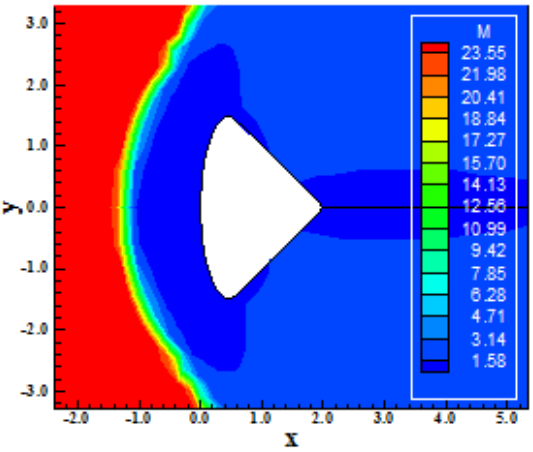

Figure 33. Mach number contours ([3]).

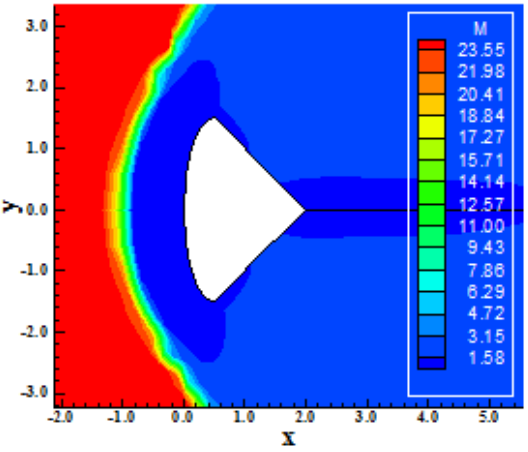

Figure 34. Mach number contours ([4]).

Figures 33 and 34 show the Mach number contours obtained by the [3-4] algorithms, respectively. Both schemes capture the wake at the capsule's trailing edge. Moreover, the flow is essentially supersonic/hypersonic and this feature is emphasized by the Mach number contours. Both schemes predict the same Mach number peak close to the body leading edge.

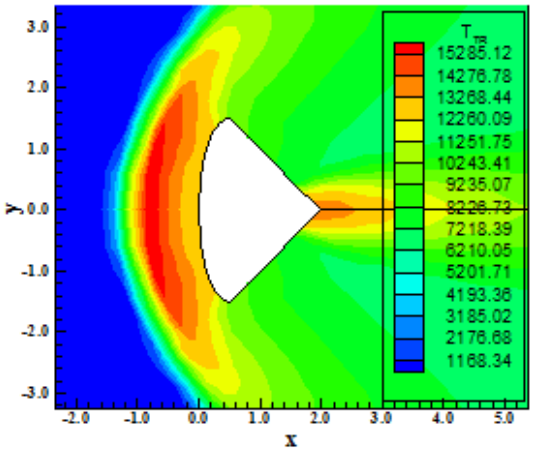

Figure 35. Translational/Rotational temperature contours ([3]).

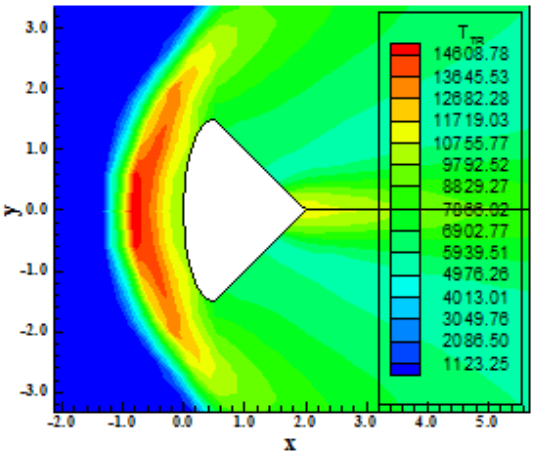

Figure 36. Translational/Rotational temperature contours ([4]).

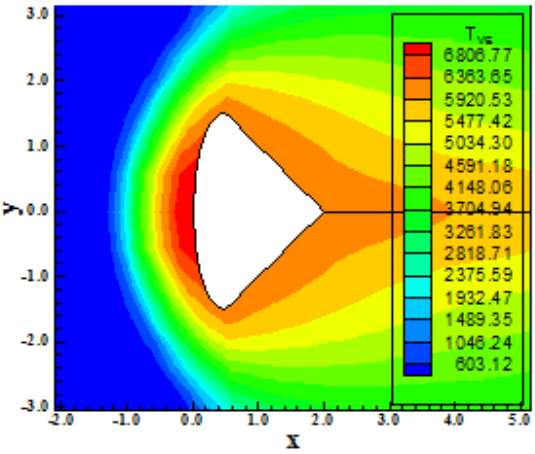

Figure 37. Vibrational temperature contours ([3]).

Figures 35 and 36 presents the translational / rotational temperature contours obtained by the [3-4]

algorithms, respectively. The temperature contours due to the [3] scheme is more intense than due to the [4] scheme. A more severe situation, with chances to yield surface melting, is highlighted with the [3] solution and attention is needed to such situation. The flow presents basically radiation heat transfer because of the high temperatures reached in this simulation. Hence, caution is required to this situation.

Figures 37 and 38 exhibit the vibrational temperature contours obtained by the [3-4] schemes, respectively. More critical vibrational temperature field is observed in the [4] solution. The vibrational temperature peak observed in the [4] solution is of the order of 8,000 K, whereas in the [3] solution is of the order of 6,800 K.

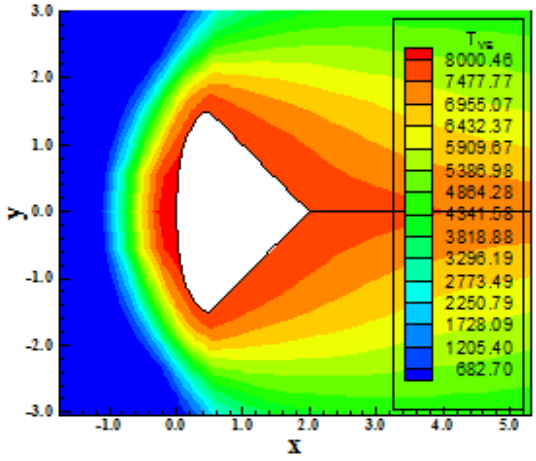

Figure 38. Vibrational temperature contours ([4]).

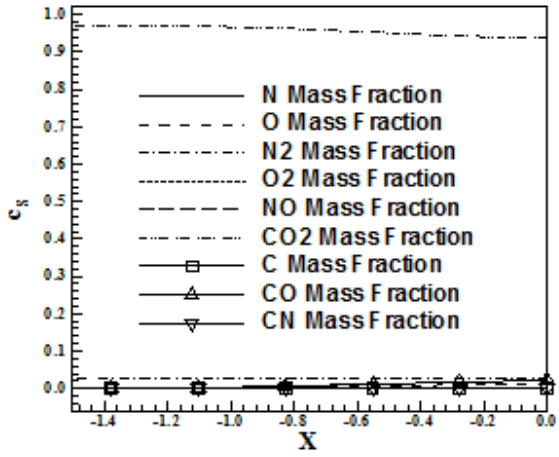

Figure 39. Species mass fraction distributions at the stagnation line ([3]).

Figure 39 exhibits the species mass fraction distributions at the stagnation line obtained by the [3] algorithm. As can be observed, a discrete dissociation of the CO_2, with a consequence discrete formation of CO and O is verified. Both dissociation of the CO_2 and formation of CO and O are inexpressive.

Figure 40 shows the species mass fraction distributions of the nine (9) species obtained by the [4] algorithm. Here, the dissociation of the CO_2 and the formation of CO and O are perceptible.

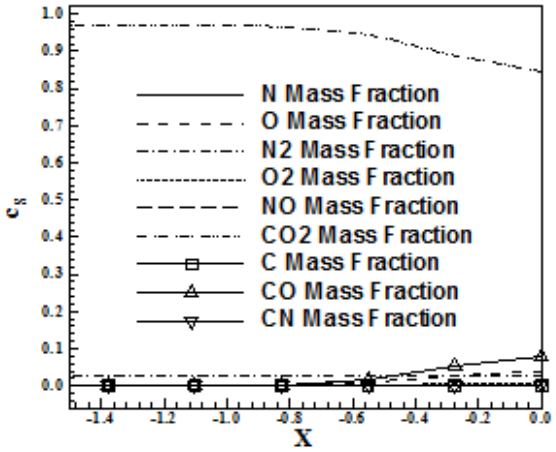

Figure 40. Species mass fraction distributions at the stagnation line ([4]).

2.2.2. Viscous, first order, structured results

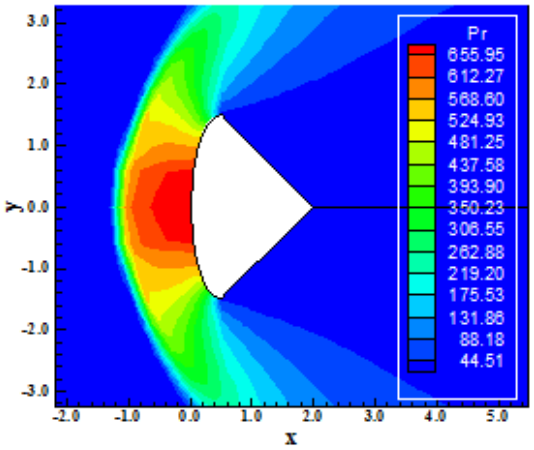

Figure 41. Pressure contours ([3]).

Figures 41 and 42 exhibit the pressure contours obtained by the [3-4] algorithms, respectively. The pressure peak is 655.95 for the [3] scheme and 639.45 for the [4] scheme. In other words, the [3] scheme is more conservative in this case. Good symmetry properties are observed in both solutions.

Figures 43 and 44 show the Mach number field generated by the [3-4] algorithms, respectively. Both schemes capture the wake at the body's trailing edge. The Mach number peak is identical for both schemes.

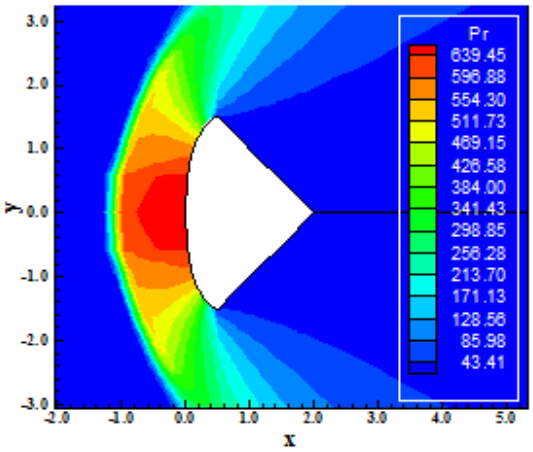

Figure 42. Pressure contours ([4]).

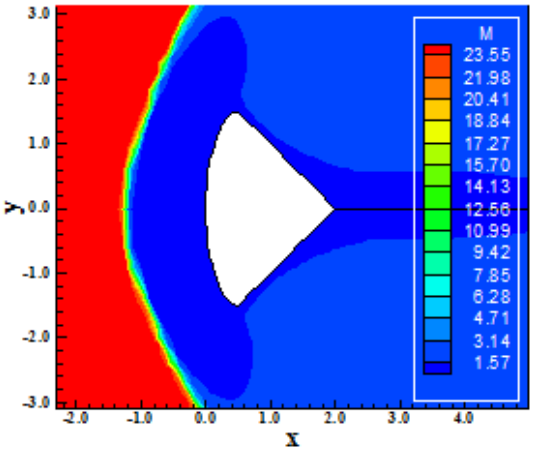

Figure 43. Mach number contours ([3]).

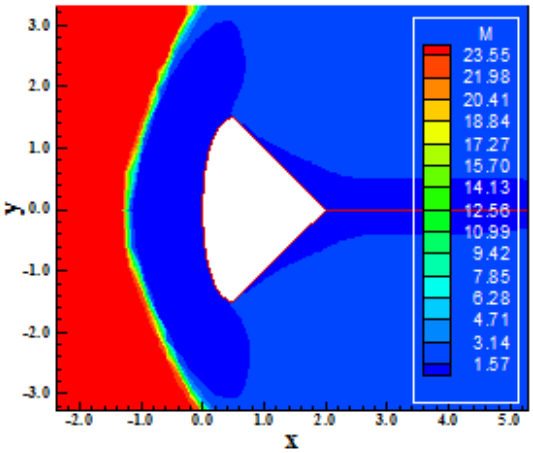

Figure 44. Mach number contours ([4]).

Figures 45 and 46 present the translational / rotational temperature contours obtained by [3-4] algorithms, respectively. The [4] scheme captures a temperature peak of the order of 32,000 K, which is wrong. On the other hand, the [3] scheme captures a more realistic temperature peak of the order of 18,000 K, for the Mars atmosphere. It seems that the [4] algorithm over-predict the temperature field at expense of reducing the vibrational temperature field.

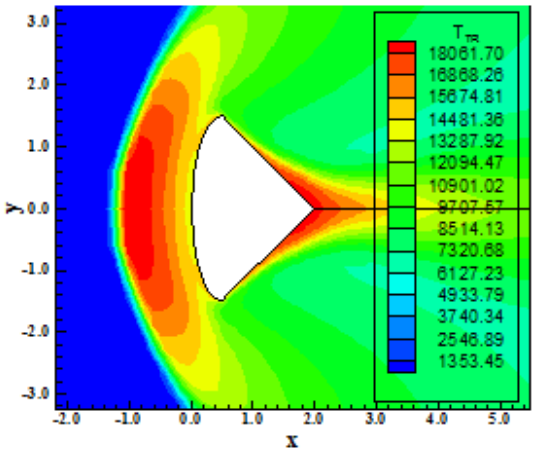

Figure 45. Translational/Rotational temperature contours ([3]).

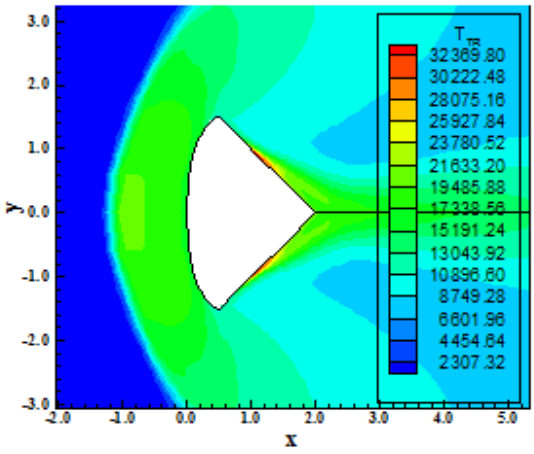

Figure 46. Translational/Rotational temperature contours ([4]).

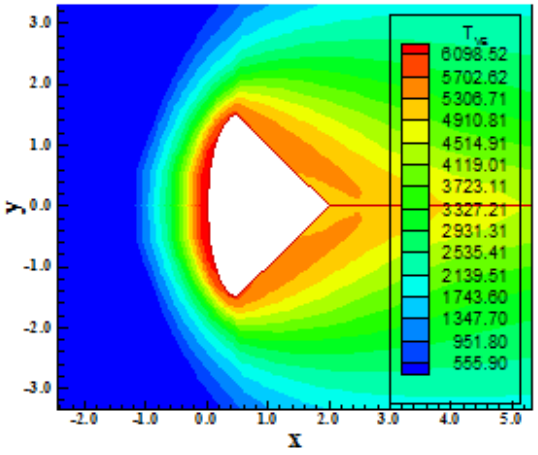

Figure 47. Vibrational temperature contours ([3]).

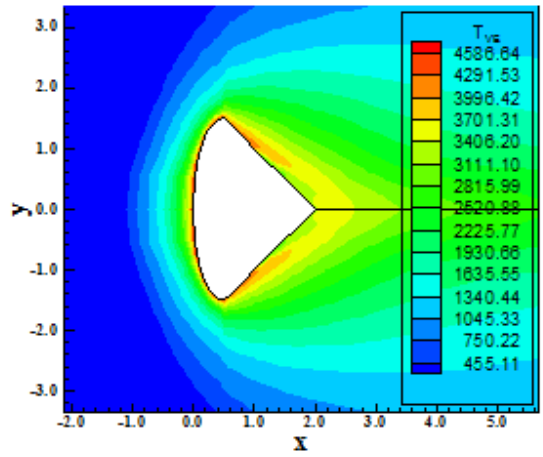

Figure 48. Vibrational temperature contours ([4]).

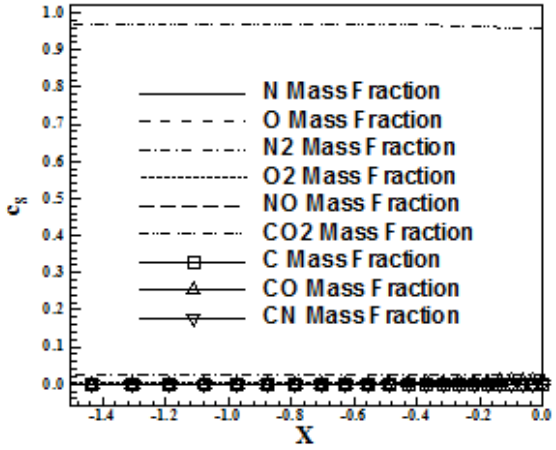

Figure 49. Species mass fraction distributions at the stagnation line ([3]).

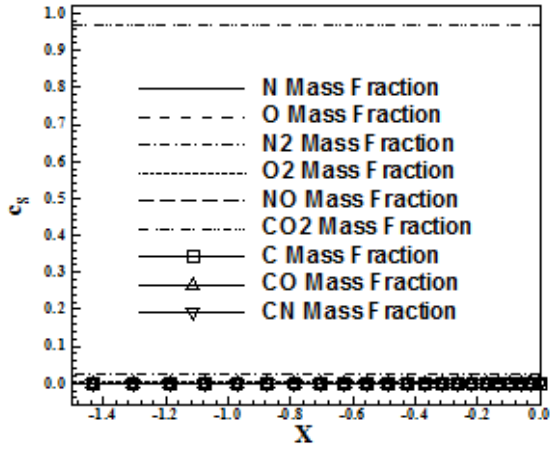

Figure 50. Species mass fraction distribution at the stagnation line ([4]).

Figures 47 and 48 present the vibrational temperature contours. The vibrational temperature field obtained by the [3] scheme is more severe than that obtained by the [4] scheme. Again, it is possible that the excessive translational/rotational temperature field results from the energy removed of the vibrational temperature field.

Figure 49 exhibits the species mass fraction distributions at the stagnation line obtained by the [3] scheme. A very discrete dissociation of CO_2 is observed close to the body's leading edge. No significant CO and O formation were captured. Figure 50 shows the same plot obtained now for the [4] solution. In this case, no dissociation is observed and, with that, there aren't CO and O formations.

2.2.3. Inviscid, second order, structured results

In this case only the [3] scheme has yielded converged results. Figure 51 exhibits the pressure contours generated by the [3] scheme. The pressure peak is equal to 602.98 unities, bigger than the respective first order inviscid solution. Good symmetry properties are observed.

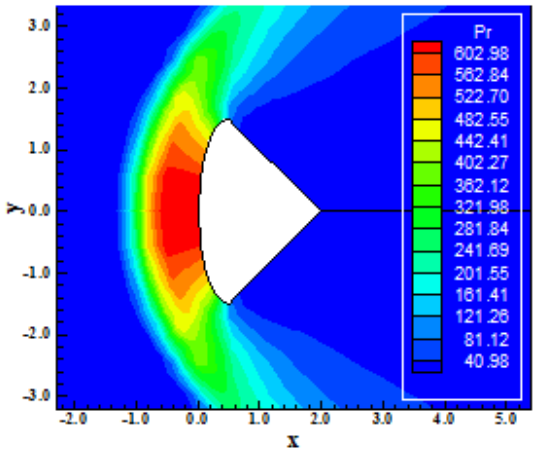

Figure 51. Pressure contours ([3]).

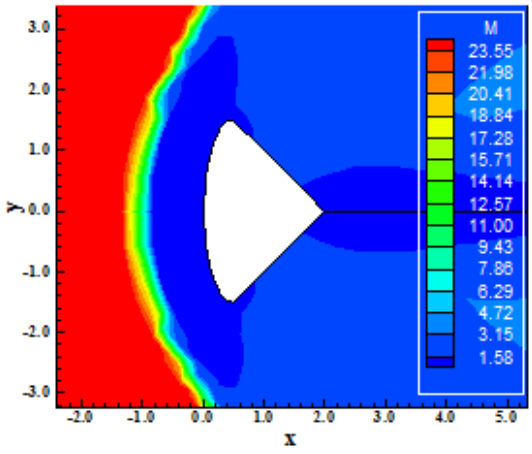

Figure 52. Mach number contours ([3]).

Figure 52 shows the Mach number contours obtained by the [3] scheme. Good symmetry properties are observed. The numerical algorithm captures appropriately the trailing edge's wake. The flow is typically supersonic and hypersonic. The Mach number peak agrees well with latter results.

Figure 53 presents the translational/rotational temperature contours generated by the [3] algorithm. The temperature peak is about 17,600 K, an expected value to the Mars atmosphere. The normal shock wave behaves as expected, with maximum intensity at the body's nose.

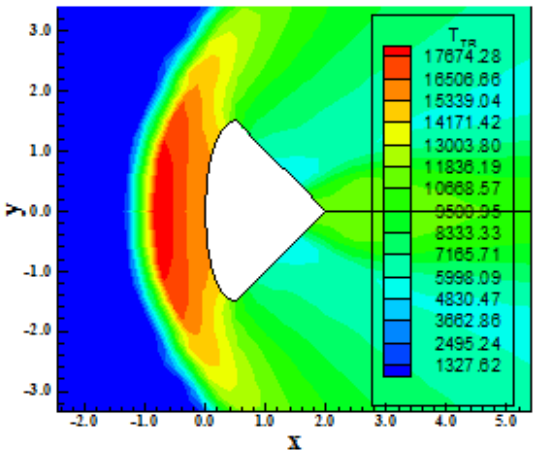

Figure 53. Translational/Rotational temperature contours ([3]).

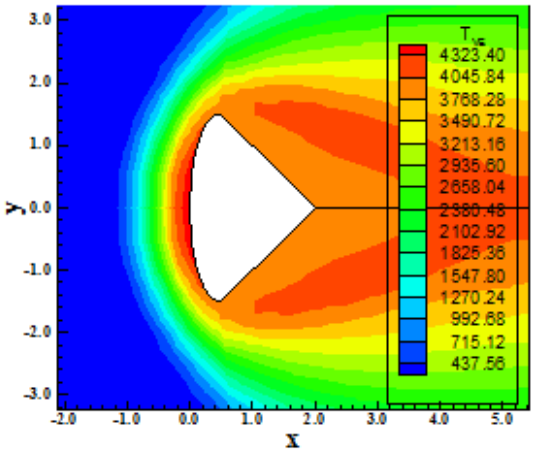

Figure 54. Vibrational temperature contours ([3]).

Figure 54 exhibits the vibrational temperature contours obtained by the [3] numerical scheme. The vibrational temperature field presents a typical behavior. Good symmetry properties are observed. According to the CFD (Computational Fluid Dynamics) literature, the translational/rotational temperature field is far greater than the vibrational temperature field, as shown in this figure.

Figure 55 presents the species mass fraction distributions at the stagnation line obtained by the [3] algorithm. No dissociation of the CO_2 is observed, resulting in no formation of CO and O.

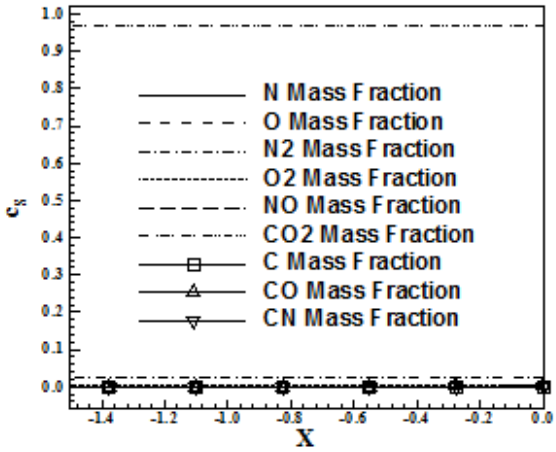

Figure 55. Species mass fraction distributions at the stagnation line ([3]).

2.2.4. Viscous, second order, structured results

Only the [3] scheme has yielded converged results for this case. Figure 56 exhibits the pressure contours. The pressure peak is of the order of 639.0 unities, lower than the respective solution obtained with the first order version of [3] algorithm. Good symmetry properties are observed.

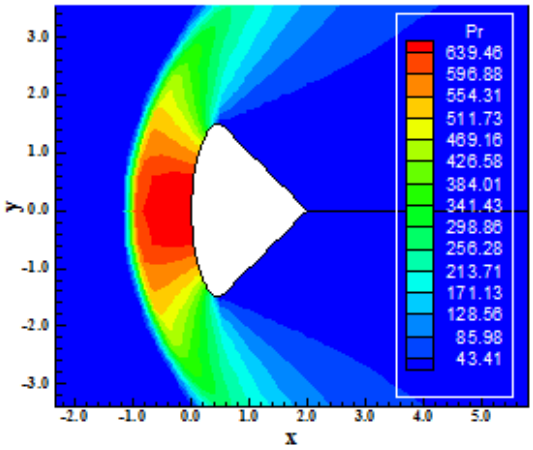

Figure 56. Pressure contours ([3]).

Figure 57 shows the Mach number contours generated by the [3] numerical algorithm. The wake is well captured, as also the shock thickness. The flow is typically supersonic and hypersonic. Good symmetry properties are observed.

Figure 58 presents the translational/rotational temperature contours obtained by the [3] scheme. The temperature peak is about 18,570 K, which was

a typical value observed in the present simulations. The biggest temperature region is found ahead of the blunt region of the entry capsule, as expected.

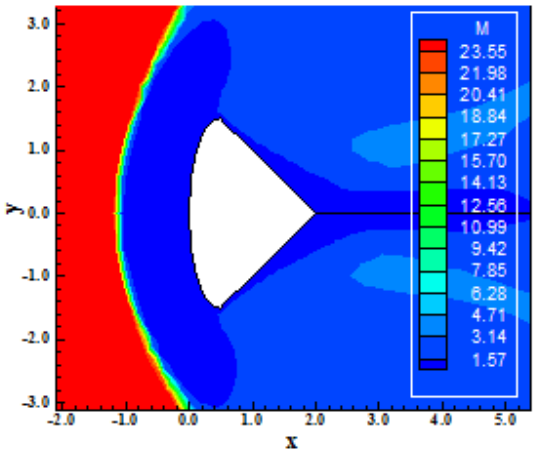

Figure 57. Mach number contours ([3]).

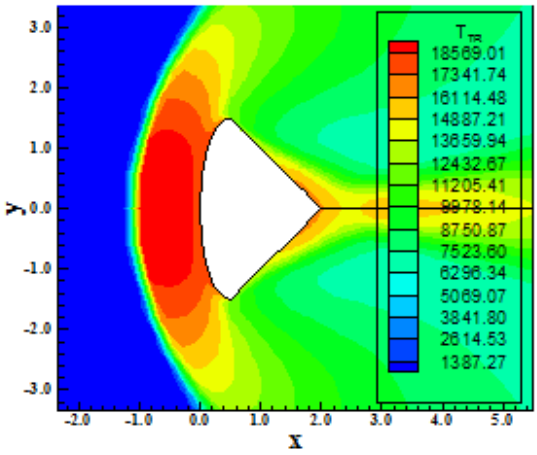

Figure 58. Translational/Rotational temperature contours ([3]).

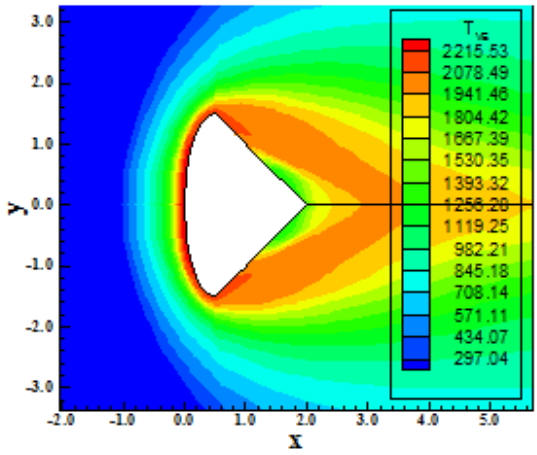

Figure 59. Vibrational temperature contours ([3]).

Figure 59 shows the vibrational temperature contours generated by the [3] algorithm. As can be noted, the vibrational temperature peak is far reduced in relation to other values of this parameter found in this study. Again, a reason to this behavior could be that the translational/rotational temperature field is keeping its tendency at the expense of reducing significantly the vibrational temperature field. The translational/rotational field is about nine (9) times bigger than the vibrational temperature, which seems very incomprehensive for the dynamics of the thermochemical non-equilibrium study performed here.

A third case is studied in this work which tries to explain such situation, which seems until this moment inconclusive. The thermochemical non-equilibrium hypersonic flow around a pathfinder is a typical study in the Martian entry problems. It was widely studied by the CFD literature. This is the next step in the present work.

Figure 60 exhibits the species mass fraction distributions of the nine (9) species at the stagnation line. As can be observed a very discrete dissociation of the CO_2 happens close to the blunt surface of the entry capsule. The formation of CO also seems to happen very close to blunt surface, but there isn't a significant formation of CO and O at the expense of dissociation of CO_2.

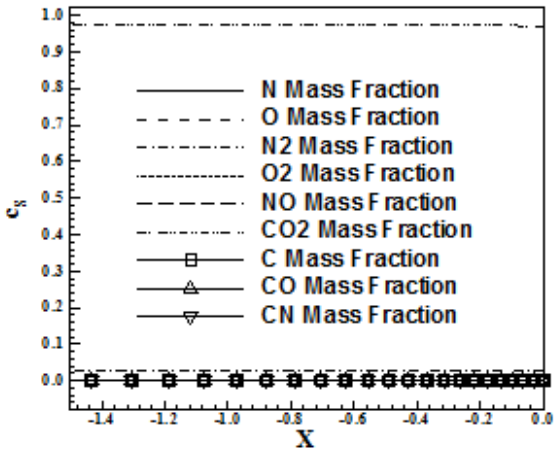

Figure 60. Species mass fraction distributions at the stagnation line ([3]).

2.3 Pathfinder Problem

The Mars Pathfinder successfully completed entry descent and landing on the Martian surface on 4 July 1997. The primary objective of the probe mission was to demonstrate a low-cost reliable system for landing in the surface of Mars. The geometry of the probe is shown in Fig. 61. The forebody is a sphere-cone shape with a nose radius of 0.66 m and a half-angle cone of 60 degrees; the afterbody is a truncated cone with a half-angle of 46

degrees. The meshes used for the numerical computations in the inviscid and viscous cases are shown in Figs. 62 and 63, respectively.

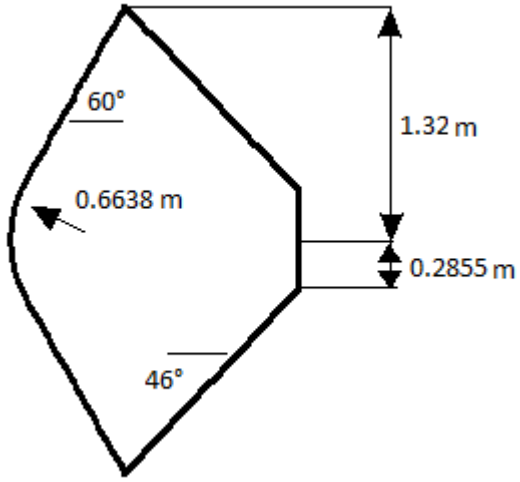

Figure 61. Pathfinder configuration.

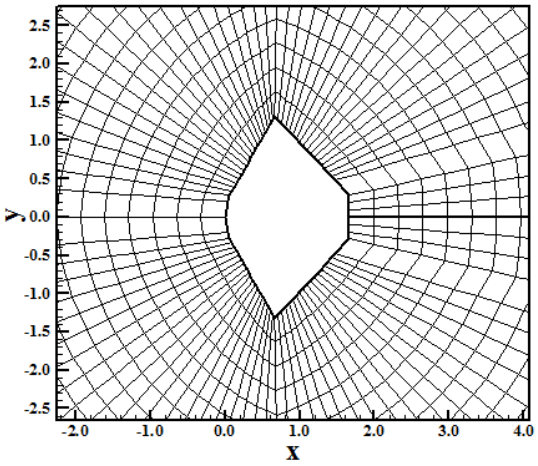

Figure 62. Pathfinder mesh (Inviscid case).

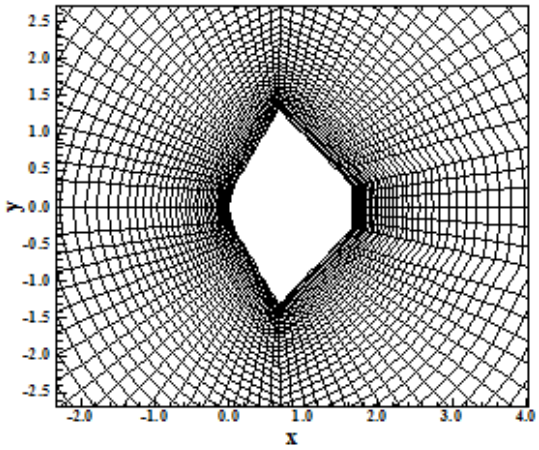

Figure 63. Pathfinder mesh (Viscous case).

The pathfinder mesh is composed of 4,956 rectangular cells and 4,250 nodes in the structured case, which correspond to a mesh of 85x60 points on a finite difference context. In the viscous case, an exponential stretching of 7.5% was employed. To the boundary conditions the reader is encouraged to read [9] and the Kutta condition described in this work. The initial condition for this problem is described in Tab. 3.

Table 3. Initial conditions to the pathfinder problem.

Property	Value
M_∞	32.0
ρ_∞	0.00028 kg/m^3
p_∞	9.2926 Pa
U_∞	6,368 m/s
T_∞	170.0 K
Altitude	41,000 m
c_N	0.00
c_O	0.00
c_{N_2}	0.05
c_{O_2}	0.00
c_{NO}	0.00
c_{CO_2}	0.95
c_C	0.00
c_{CO}	0.00
c_{CN}	0.00
L	2.64 m
Re_∞	5.19x10^5

2.3.1. Inviscid, first order, structured results

In this sub-section, it will be highlighted the inviscid and first order solutions obtained by the [3] and [4] schemes to the pathfinder configuration problem.

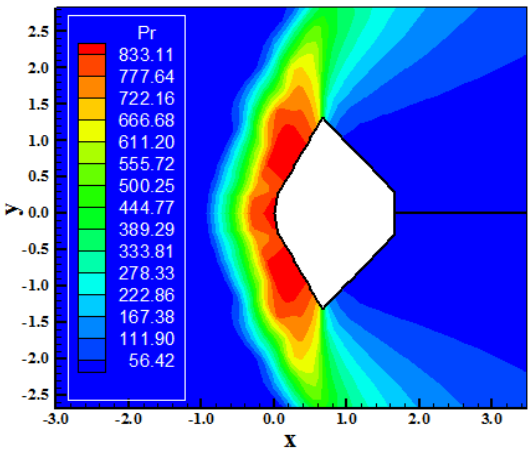

Figure 64. Pressure contours ([3]).

Figures 64 and 65 exhibit pressure contours obtained by the [3] and [4] schemes, respectively. The maximum pressure field is captured by the [4] algorithm. Good symmetry properties are observed.

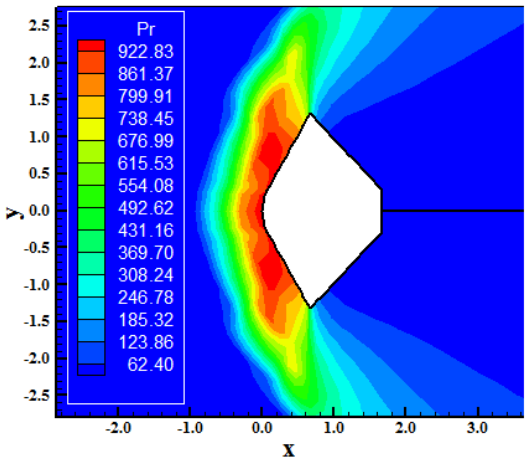

Figure 65. Pressure contours ([4]).

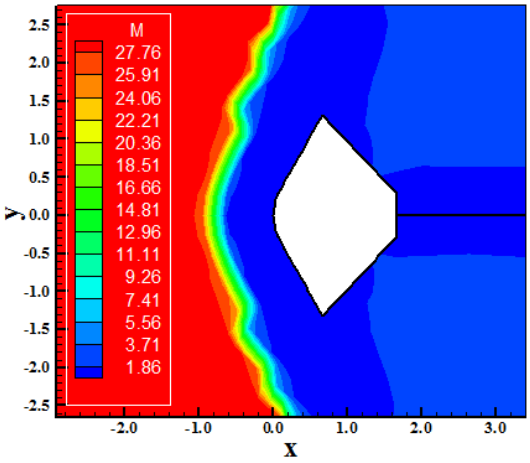

Figure 66. Mach number contours ([3]).

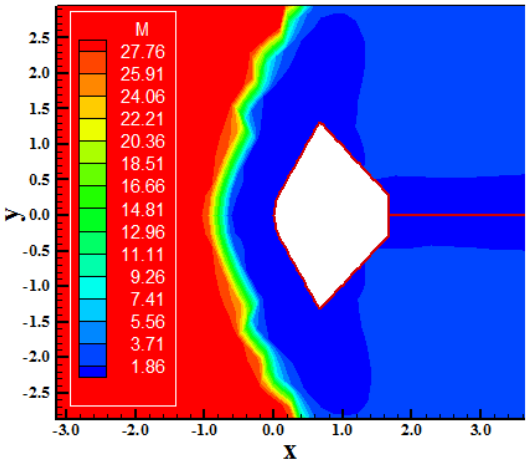

Figure 67. Mach number contours ([4]).

Figure 66 and 67 show Mach number contours generated by the [3] and [4] schemes, respectively. The supersonic region is bigger in the [3] solution. The Mach number field is equal to both solutions in quantitative terms.

Figures 68 and 69 present translational/rotational temperature contours obtained by the [3] and [4] algorithms, respectively. The [3] solution presents a bigger temperature field than the [4] solution. The maximum temperature region is found in the [3] solution.

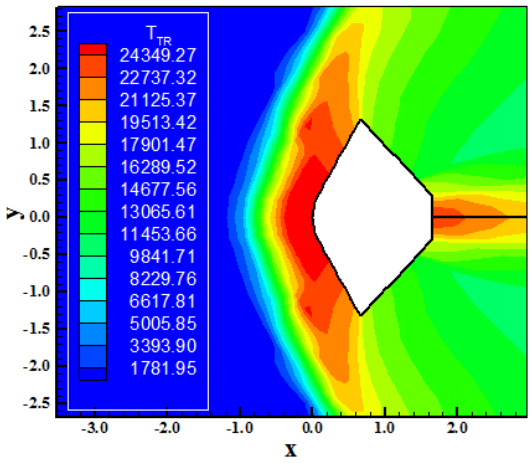

Figure 68. Translational/Rotational temperature contours ([3]).

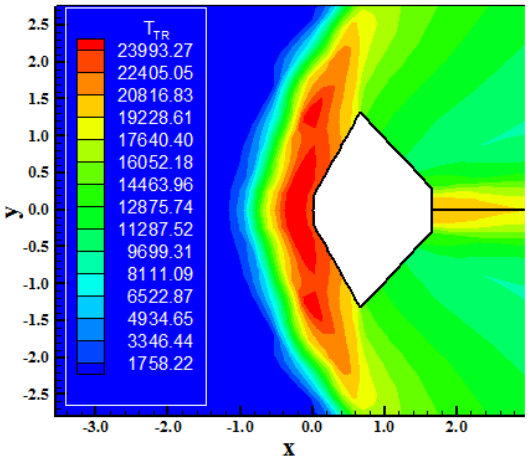

Figure 69. Translational/Rotational temperature contours ([4]).

Figures 70 and 71 exhibit vibrational temperature contours obtained by the [3] and [4] schemes, respectively. The maximum vibrational temperature field is obtained in the [4] solution, whereas the [3] solution presents a bigger region of high vibrational temperature field.

Figure 72 shows the mass fraction distributions obtained by the nine (9) species along the body's stagnation line, generated by the [3] scheme. As can be observed, the formation of CO and of O is very

discrete. The CO_2 dissociation is small. Figure 73 presents the mass fraction distributions obtained by the nine (9) species along the body's stagnation line, generated by the [4] scheme. The CO_2 dissociation is more perceptible. The CO formation is slightly observed.

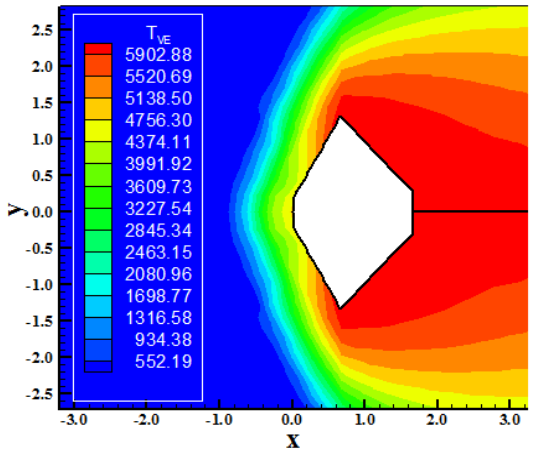

Figure 70. Vibrational temperature contours ([3]).

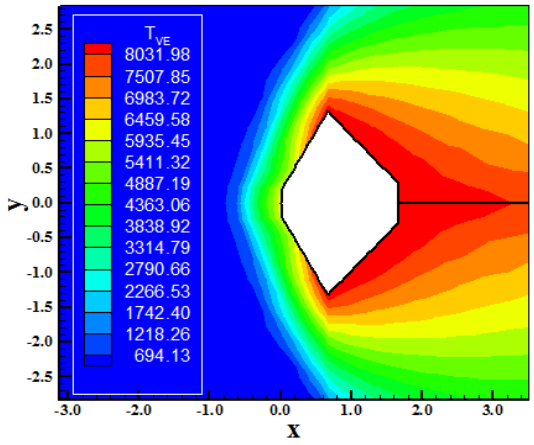

Figure 71. Vibrational temperature contours ([4]).

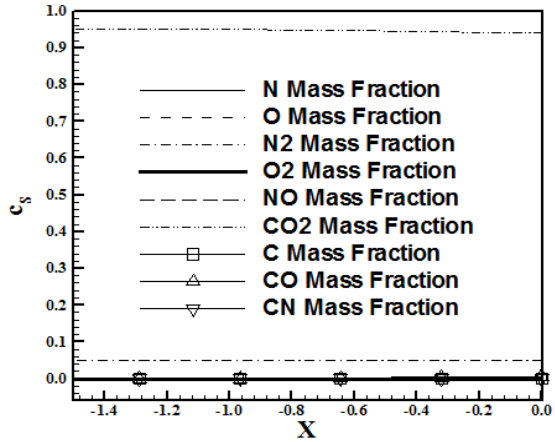

Figure 72. Species mass fraction distributions at the stagnation line ([3]).

In this study, it is perceptible that the vibrational temperature is only four (4) times smaller than the translational/rotational temperature, in its worst case, what means that the capsule entry results are something out of reality. Maybe, the mesh generation process could be improved, resulting in a better description of the geometry and a more realistic simulation.

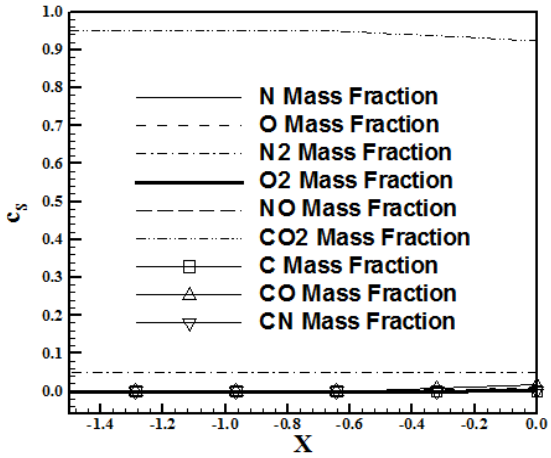

Figure 73. Species mass fraction distributions at the stagnation line ([4]).

2.3.2. Viscous, first order, structured results

To the viscous simulations, a Reynolds number equal to 5.19×10^5 was employed. No turbulence model was employed, although the Reynolds number is sufficient large to justify such flow regime.

Figures 74 and 75 exhibit the pressure contours obtained by [3] and [4], respectively. The main feature of the viscous simulation is to recover the normal shock wave characteristics, which had been lost in the inviscid simulations, The exponential stretching introduces a better capture of the shock wave at the configuration nose.

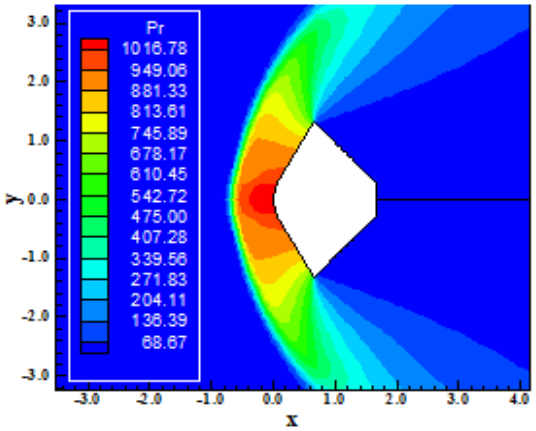

Figure 74. Pressure contours ([3]).

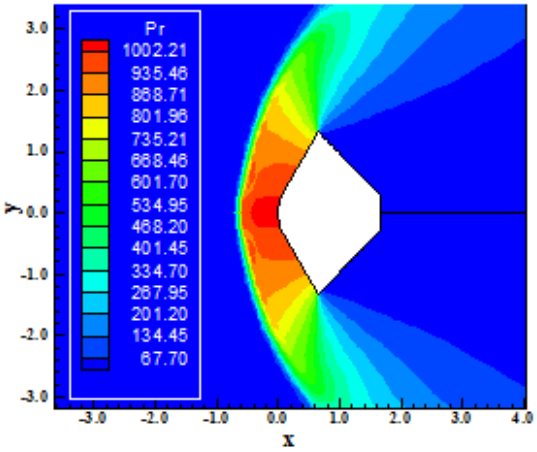

Figure 75. Pressure contours ([4]).

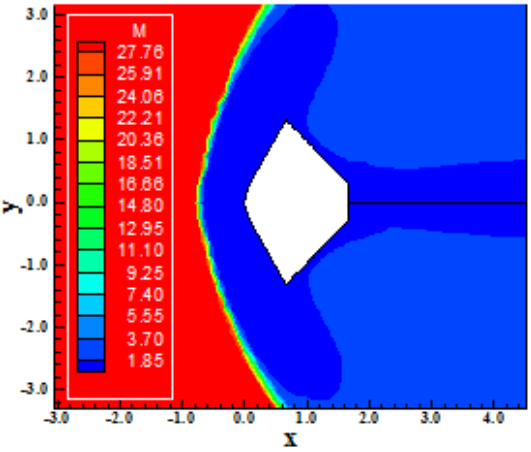

Figure 76. Mach number contours ([3]).

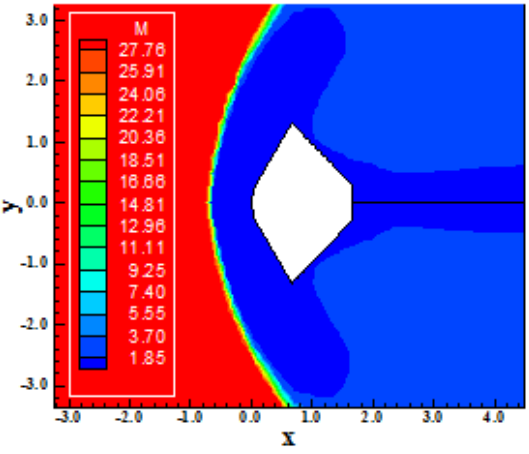

Figure 77. Mach number contours ([4]).

Figures 76 and 77 show the Mach number contours obtained by [3] and [4], respectively. Both solutions present good symmetry characteristics. The Mach number fields, in quantitative terms, present good similarity.

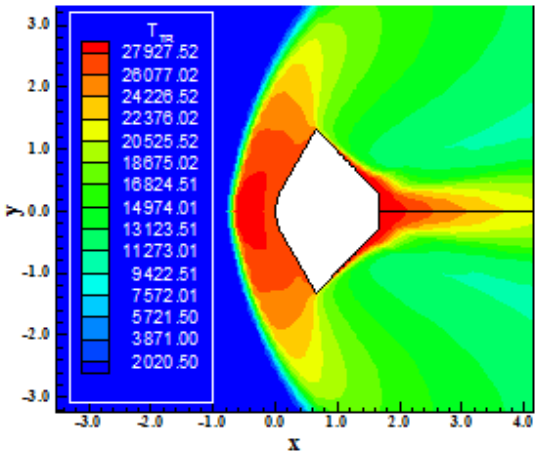

Figure 78. Translational/Rotational temperature contours ([3]).

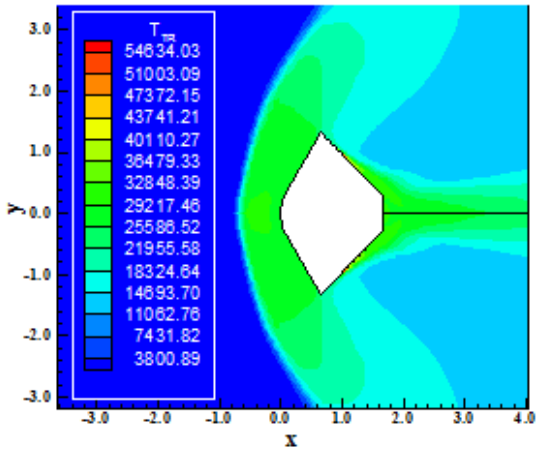

Figure 79. Translational/Rotational temperature contours ([4]).

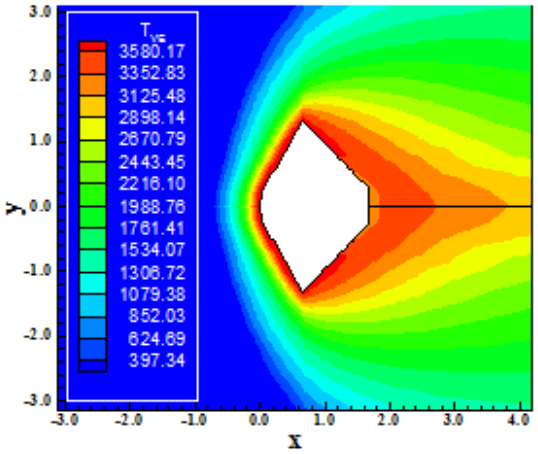

Figure 80. Vibrational temperature contours ([3]).

Figures 78 and 79 exhibit the translational / rotational temperature contours obtained by the [3] and the [4] schemes, respectively. An appropriated

capture of normal shock wave and the determination of the translational/rotational temperature peak region is a meaningful gain of the [3] scheme. The [4] scheme over-predicts the translational/rotational temperature field in relation to the [3] scheme. In words, there is a non-physical behavior detected by the [4] scheme, which damages its solution quality.

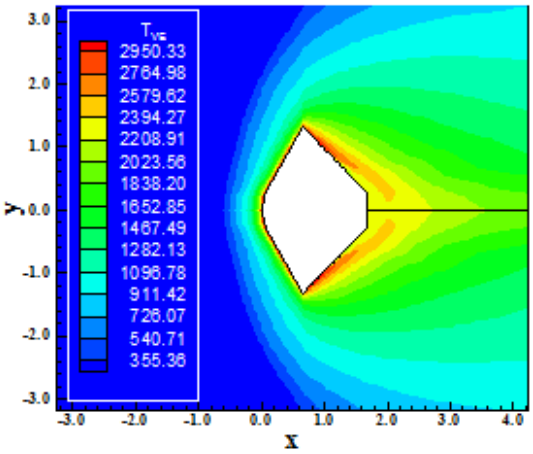

Figure 81. Vibrational temperature contours ([4]).

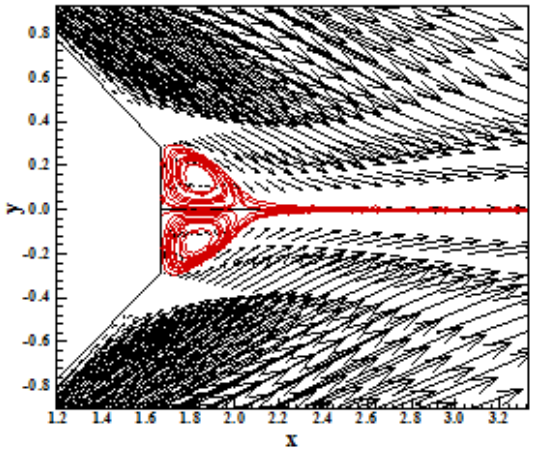

Figure 82. Streamlines and circulation bubbles ([3]).

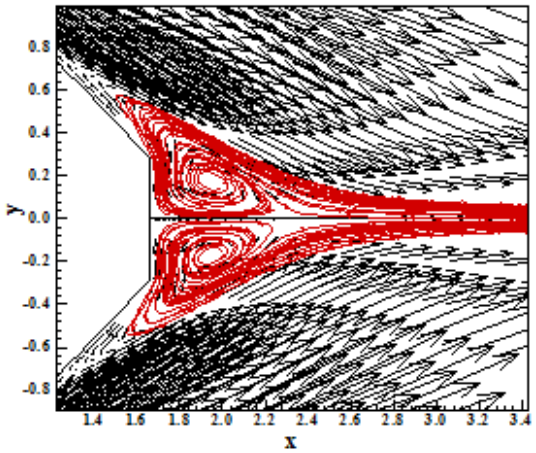

Figure 83. Streamlines and circulation bubbles ([4]).

Figures 80 and 81 show the vibrational temperature contours obtained by the [3] and the [4] schemes, respectively. As can be seen, the best vibrational temperature distribution is captured by the [3] scheme. The solution presented by the [4] scheme is very discrete and the jump in terms of translational / rotational temperature to vibrational temperature ratio is very large to the [4] scheme (about 18.5 times bigger). Observe that the [3] presents such ratio with a value of 7.8, a value relatively reasonable.

Figures 82 and 83 present the streamlines at the trailing edge of the configuration. A circulation bubble is formed at the forebody of the configuration, due to boundary layer detachment. The pair of vortices is bigger in the solution of the [4] scheme, although more symmetrical structures are obtained by the [3] scheme.

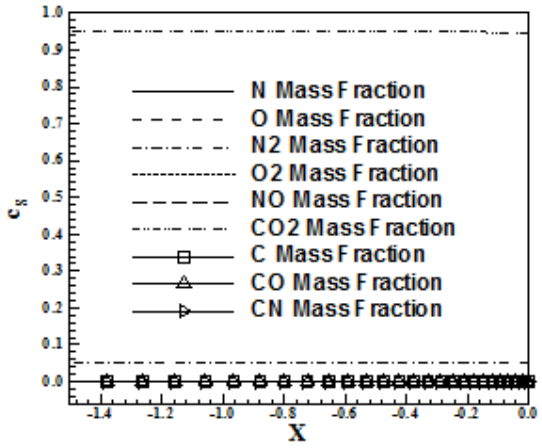

Figure 84. Species mass fraction distributions at the stagnation line ([3]).

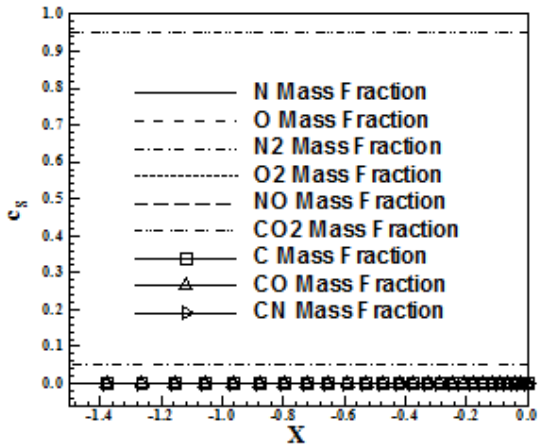

Figure 85. Species mass fraction distributions at the stagnation line ([4]).

Figure 84 presents the mass fraction distribution at the stagnation line, close to the body's leading edge, generated by the [3] scheme. As can be observed, there is a small dissociation of the CO_2, with consequent discrete formations of the other molecules and atoms. In Figure 85 less dissociation of the CO_2 occurs, resulting in less formation of atoms and other molecules.

2.3.3. Viscous, second order, structured results

For second order results, only the viscous and structured case with the [3] algorithm has yielded converged solutions. The second order inviscid solutions of this algorithm yielded convergence until the residual has dropped 2.7 magnitude orders and after that the convergence has stagnated.

The pressure contours obtained by the [3] scheme is presented in Fig. 86. Good symmetry properties are observed in this solution. The region ahead of the configuration nose presents good description of the flowfield, characterizing the expected behaviour to the contours lines, similar to the blunt body symmetry lines, described in [9].

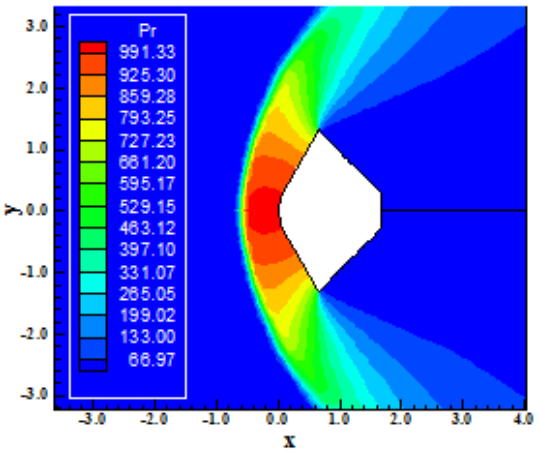

Figure 86. Pressure contours ([3]).

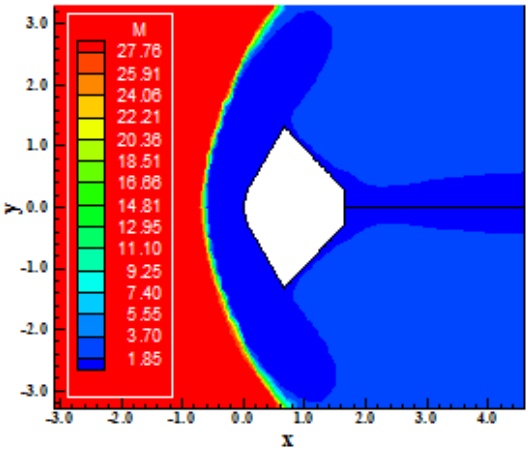

Figure 87. Mach number contours ([3]).

Figure 87 presents the Mach number contours obtained by the second order TVD scheme of [3]. The normal shock wave is well captured, as also the region of supersonic flow behind the wave. A wake is formed at the pathfinder's trailing edge.

Figure 88 shows the translational/rotational temperature contours obtained by the second order scheme of [3]. The maximum temperature reached in these simulations was 27,689 K, which is in accordance with other simulations performed by the authors.

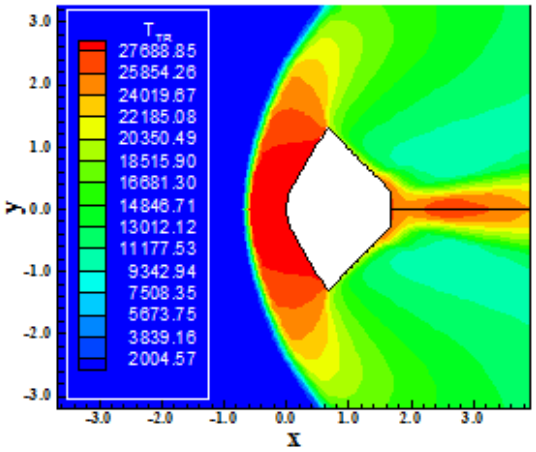

Figure 88. Translational/rotational temperature contours ([3]).

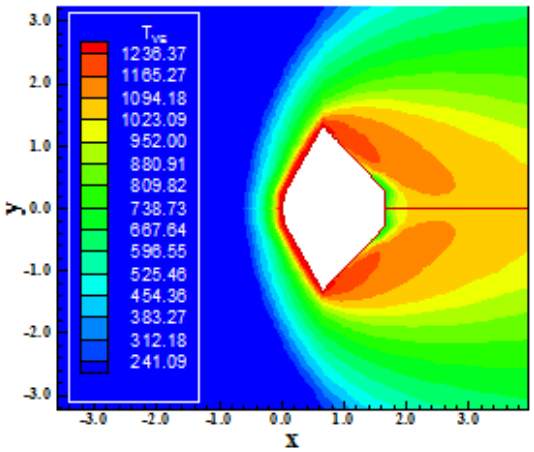

Figure 89. Vibrational temperature contours ([3]).

Figure 89 exhibits the vibrational temperature contours obtained by the [3] scheme. The peak of vibrational temperature is 1,236 K, which corresponds to the translational/rotational temperature 22.0 times bigger than the vibrational temperature. The solution presents good symmetry properties and the peak of vibrational temperature is found at the configuration nose.

Figure 90 presents the velocity vector field with streamlines highlighting the pair of vortices formed

at the pathfinder's trailing edge. As can be noted, a pair of vortices is developed at the detached boundary layer region, close to the geometry's trailing edge. This pair of vortices spreads downward along the wake generated at the geometry's trailing edge.

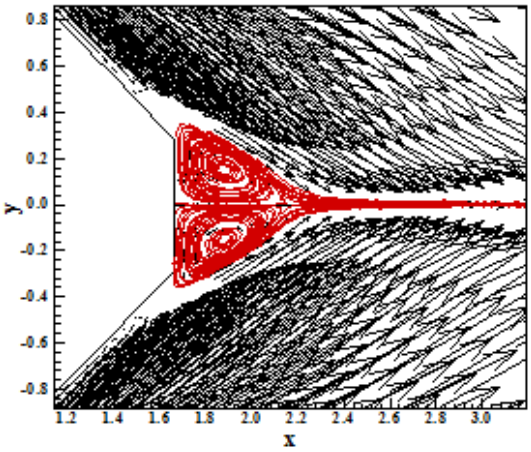

Figure 90. Streamlines and circulation bubbles ([3]).

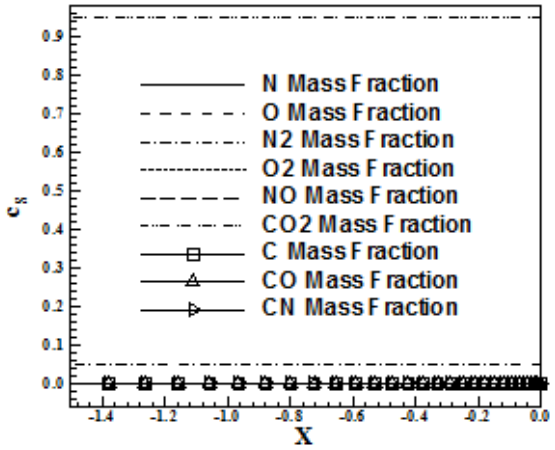

Figure 91. Species mass fraction distributions at the stagnation line ([3]).

Figure 91 exhibits the species mass fraction distributions of the nine species along the stagnation line. As can be observed, the dissociation of CO_2 is very discrete. The CO and O is the result of the CO_2 dissociation. The CN has negligible mass fraction in the stagnation line and in the field.

2.4 Lift and drag coefficients

Table 4 presents the aerodynamic coefficients of lift and drag to the entry capsule and to the pathfinder. Due to symmetric geometry, these configurations generate zero lift coefficients to the studied problems. Hence, these values serve as a measure of the numerical algorithms accuracies. As can be observed, the best solution was obtained with the [3] scheme, inviscid and first order case, to the pathfinder problem. The biggest drag coefficient was due to the [4] scheme, first order and viscous case, to the pathfinder problem.

Table 4. Aerodynamic coefficients of lift and drag.

Problem	Case	c_L	c_D
Entry Capsule	[3] – $I^{(1)}$ – 1st	2.21×10^{-10}	2.07
	[4] – I – 1st	-2.00×10^{-8}	2.20
	[3] – I – 2nd	7.09×10^{-10}	2.08
	[3] – $V^{(2)}$ – 1st	7.76×10^{-10}	2.30
	[4] – V – 1st	3.29×10^{-10}	2.26
	[3] – V – 2nd	-2.07×10^{-10}	2.23
Pathfinder	[3] – I – 1st	-1.77×10^{-11}	2.09
	[4] – I – 1st	-2.63×10^{-10}	2.25
	[3] – V – 1st	6.93×10^{-10}	2.39
	[4] – V – 1st	1.06×10^{-9}	2.45
	[3] – V – 2nd	-1.11×10^{-9}	2.39

(1): Inviscid; (2): Viscous.

3 Conclusions

This work, second part of this study, describes the numerical results obtained by thermochemical non-equilibrium simulations of reactive flow in two-dimensions. The [3-4] schemes, in their first- and second-order versions, are implemented to accomplish the numerical simulations. The Euler and Navier-Stokes equations, on a finite volume context and employing structured spatial discretization, are applied to solve the "hot gas" hypersonic flows around a double ellipse and around an entry capsule, in two-dimensions. A third configuration, the pathfinder, is also studied trying to elucidate some doubts in relation to the ratio translational/rotational temperature and vibrational temperature. The second-order versions of the [3-4] schemes are obtained from a "MUSCL" extrapolation procedure (details in [5]) in a context of structured spatial discretization. The convergence process is accelerated to the steady state condition through a spatially variable time step procedure, which has proved effective gains in terms of computational acceleration (see [6-7]).

The reactive simulations involve a Mars atmosphere chemical model of nine species: N, O, N_2, O_2, NO, CO_2, C, CO, and CN. Fifty-three chemical reactions, involving dissociation and recombination, are simulated by the proposed model. The Arrhenius formula is employed to determine the reaction rates and the law of mass action is used to

determine the source terms of each gas species equation.

The results have demonstrated that the most correct aerodynamic coefficient of lift is found in the pathfinder problem with the [3] scheme, first-order accurate, in an inviscid formulation, to a reactive condition of thermochemical non-equilibrium.

The two papers described along this work do part of a more global study involving re-entry flows in Earth and entry flows in Mars. To the reader becomes familiar with this global study, the following references are indicated to: [10-12].

4 Acknowledgments

Both authors acknowledge the infra-structure of the ITA that allowed the realization of this work.

References:

[1] ESA, MARSNET – Assessment Study Report, *ESA Publication SCI* (91) 6, January, 1991.

[2] E. S. G. Maciel, and A. P. Pimenta, Thermo-chemical Non-Equilibrium Reentry Flows in Two-Dimensions – Part I, *WSEAS Transactions on Mathematics*, Vol. 11, Issue 6, June, 2012, pp. 520-545.

[3] B. Van Leer, Flux-Vector Splitting for the Euler Equations, *Lecture Notes in Physics*. Springer Verlag, Berlin, Vol. 170, 1982, pp. 507-512.

[4] M. Liou, and C. J. Steffen Jr., A New Flux Splitting Scheme, *Journal of Computational Physics*, Vol. 107, 1993, pp. 23-39.

[5] C. Hirsch, Numerical Computation of Internal and External Flows – Computational Methods for Inviscid and Viscous Flows. John Wiley & Sons Ltd, 691p, 1990.

[6] E. S. G. Maciel, Analysis of Convergence Acceleration Techniques Used in Unstructured Algorithms in the Solution of Aeronautical Problems – Part I, *Proceedings of the XVIII International Congress of Mechanical Engineering (XVIII COBEM)*, Ouro Preto, MG, Brazil, 2005. [CD-ROM]

[7] E. S. G. Maciel, Analysis of Convergence Acceleration Techniques Used in Unstructured Algorithms in the Solution of Aerospace Problems – Part II, *Proceedings of the XII Brazilian Congress of Thermal Engineering and Sciences (XII ENCIT)*, Belo Horizonte, MG, Brazil, 2008. [CD-ROM]

[8] NASA, Models of Mars' Atmosphere [1974], *NASA SP-8010*.

[9] E. S. G. Maciel, and A. P. Pimenta, Thermochemical Non-Equilibrium Entry Flows in Mars in Two-Dimensions Part I, *WSEAS Transactions on Applied and Theoretical Mechanics*, Vol. 8, Issue 1, January, 2013, pp. 26-54.

[10] E. S. G. Maciel, and A. P. Pimenta, Thermochemical Non-Equilibrium Reentry Flows in Two-Dimensions – Part II, *WSEAS Transactions on Mathematics*, Vol. 11, Issue 11, November, 2012, pp. 977-1005.

[11] E. S. G. Maciel, and A. P. Pimenta, Thermochemical Non-Equilibrium Reentry Flows in Two-Dimensions: Seven Species Model – Part I, *WSEAS Transactions on Applied and Theoretical Mechanics*, Vol. 7, Issue 4, October, 2012, pp. 311-337.

[12] E. S. G. Maciel, and A. P. Pimenta, Thermochemical Non-Equilibrium Reentry Flows in Two-Dimensions: Seven Species Model – Part II, *WSEAS Transactions on Applied and Theoretical Mechanics*, Vol. 8, Issue 1, January, 2013, pp. 55-83.